

# MSS RESEARCH LETTERS

Issue #5, July 2020

---

**DISCLAIMER OF WARRANTIES AND LIABILITY**

1. While National Environment Agency Meteorological Service Singapore (NEA MSS) has made every reasonable effort to ensure that the information contained in this publication has been obtained from reliable sources, NEA MSS shall not be responsible for any errors or omissions, or for the results obtained from the use of such information.
2. NEA MSS shall also not be liable for any damage or loss of any kind howsoever caused as a result of any reliance on the contents of this publication.

---

## EDITOR'S NOTE.

Dear Readers,

I am happy to present the fifth issue of MSS Research Letters. This is the first issue of 2020, a year that has been filled with lots of uncertainties, anxieties and hurdles. On a positive note, however, we have found our own ways to handle the tough moments and to adapt ourselves to this 'new normal'. There is still a long way to go, and I believe that each one of us will definitely sail through this storm.

The fifth issue of MSS research Letters presents four letters. Three of the four letters have been contributed by CCRS and WSD staff. The first letter covers the evaluation of MSS' in-built SINGV-DA's short-range forecasts of precipitation and lower tropospheric atmospheric conditions over Singapore over the meteorological year December 2018 to November 2019. The second letter is on the detection of hotspots by satellite products on the islands of Sumatra and Borneo and the verification of the results. The third letter speaks about the impact of transboundary haze on surface solar irradiance in Singapore. The final letter is about anthropogenic heat flux emission for Singapore, and is a part of a collaborative project between CCRS and the National University of Singapore, called: 'Role of urbanization on the diurnal cycle of rainfall over Singapore'.

Through this issue I also take pleasure in welcoming our new Director of CCRS, Dr Dale Barker, who will be joining us in August. Welcome, Dale!

I would also like to thank the authors and reviewers of this issue, who in spite of the difficult and 'new' working conditions, made sure to provide their contributions, comments and revisions. My sincere acknowledgement goes to Micheline who has been helping me through the various stages of the editorial tasks of the MSS Research Letters. Thanks a lot Micheline!

Enjoy this issue of MSS Research Letters, and I am looking forward to having more contributions in the next issues. 😊

Take care and stay safe,  
Hindumathi Palanisamy  
Editor, MSS Research Letters

*Cover figures: top left – 12-hour Island wide averaged PM10 concentration from 2010 to 2016. PM10 concentrations of 25, 50 and 75  $\mu\text{g m}^{-3}$  are marked with horizontal dashed lines (Page 25); bottom left – Hourly anthropogenic heat flux [ $\text{W m}^{-2}$ ] from all individual sectors in Singapore (Page 37); bottom right – Number of detected hotspots per island for January and July 2019, including missed detections, correct detections and non-verifiable detections (Page 19); top right - The SINGV-DA domain, with model orography shaded and a zoomed-in view of the area around Singapore in the inset (Page 6).*

---

# TABLE OF CONTENTS

1. Verification of SINGV-DA forecasts over Singapore (December 2018 to November 2019) 5  
Boon Chong Peter Heng, Xiang-Yu Huang (CCRS)  
SINGV-DA is a convective-scale numerical weather prediction (NWP) system developed specifically for Singapore and the surrounding region. As with any operational NWP system, forecast verification is a crucial activity, both to monitor model performance and to spur further development. This article presents an objective evaluation of SINGV-DA's short-range forecasts of precipitation and lower tropospheric atmospheric conditions over Singapore over the meteorological year December 2018 to November 2019, benchmarked against the European Centre for Medium-Range Weather Forecasts (ECMWF) High Resolution (HRES) global model. We found that SINGV-DA's performance varied between seasons, and that this seasonal variation is partly attributable to the driving model. Compared to the global model, which has a tendency to over-(under-) forecast light (heavy) rain events, SINGV-DA's precipitation forecasts are markedly more realistic.
  
2. Preliminary evaluation of the NOAA-20/JPSS-1 Active Fires 750m satellite product in Sumatra and Borneo using Sentinel-2 satellite data 15  
Efthymia Pavlidou, Songhan Wong (WSD)  
Timely detection and monitoring of active forest and land fires are crucial and challenging for Southeast Asia, considering the ecosystem complexity and the severity of fire and smoke haze impacts in the region. Global satellite-based products are operationally available but need to be assessed, and potentially adjusted, to address local conditions. In this study, hotspots detected by the NOAA-20/JPSS-1 Active Fires operational product suite are verified in wet and dry months (January and July 2019) in fire-prone areas of Sumatra and Borneo in Southeast Asia. Given the scarcity of ground-based data, verification is based on high spatial resolution optical imagery from Sentinel-2 allowing for detailed visual examination of the study areas. Furthermore, Fire Radiative Power (FRP) estimates from the NOAA-20/JPSS-1 Active Fires product suite are examined along with the Confidence Levels reported for the detections. High Precision scores are found overall ( $> 0.70$ ), indicating that the majority of reported hotspots in NOAA-20/JPSS-1 Active Fires corresponded to actual fires seen in Sentinel-2. However, the number of missed detections was almost as high as the number of reported hotspots. Common reasons for missed detections are cloud cover and the presence of smoke obscuring burning areas. When higher Confidence Levels of reported hotspots are considered, hotspot detection performance improves. At the same time, high Confidence Levels coincide already with fires of low estimated FRP, indicating a potential for early fire detection. Finally, the study demonstrates an approach to quantitatively considering Confidence Levels in order to optimise utilisation of the product for decision-making.
  
3. Understanding the impact of transboundary haze on surface solar irradiance in Singapore 25  
Chia Zhong Yi, Christopher Gan (CCRS)  
During transboundary haze episodes, local visibility in Singapore is often reduced due to visible light scattering by airborne haze particles. This scattering also affects the transmissivity of the atmosphere, which implies that solar irradiance received by solar panels is affected by the presence of airborne haze particles. To investigate the impact of haze on the transmissivity of the atmosphere, the statistical distributions of clearness index (the transmissivity of the atmosphere) during hazy and non-hazy days were compared. A two-sample Kolmogorov-Smirnov (K-S) test demonstrated that haze particles do affect the transmissivity of the atmosphere. However, the analysis showed that even during hazy periods, cloud cover remains an important factor in solar forecasting. The findings suggest that an effective solar forecasting system for hazy periods must be able to predict both haze particle concentrations and cloud spatial distributions reliably.

4. An anthropogenic heat flux emission inventory for Singapore for urban climate modelling 34  
Andrés Simón-Moral, Matthias Roth (NUS)

An inventory-based anthropogenic heat flux (QF) database is estimated for Singapore for 2016. A combination of top-down and bottom-up approaches is used to estimate the hourly QF from residential and non-residential buildings, light and heavy industry, road traffic and railway network. A diurnal profile is further calculated and applied to the entire urban area to obtain the diurnal cycle of QF. The results are calculated for a 300 m resolution grid and are ready to be implemented in the MORUSES urban canopy model. Industry is found to be the sector with the highest emissions, with maximum hourly cell values of  $300 \text{ W m}^{-2}$  and  $3500 \text{ W m}^{-2}$  from light and heavy industry, respectively. The second highest emitting sector is non-residential buildings, which can reach maximum hourly grid values of  $350 \text{ W m}^{-2}$  in the central business district. Emissions from residential buildings scale with density and height of buildings, reaching up to  $30 \text{ W m}^{-2}$  in individual cells. The road transport sector reaches maximum hourly cell values of  $60 \text{ W m}^{-2}$  in areas with expressways and the railway network emits up to  $4 \text{ W m}^{-2}$ .

Glossary

43



# Verification of SINGV-DA forecasts over Singapore (December 2018 to November 2019)

Boon Chong Peter Heng, Xiang-Yu Huang

Centre for Climate Research Singapore, Meteorological Service Singapore

## ABSTRACT

SINGV-DA is a convective-scale numerical weather prediction (NWP) system developed specifically for Singapore and the surrounding region. As with any operational NWP system, forecast verification is a crucial activity, both to monitor model performance and to spur further development. This article presents an objective evaluation of SINGV-DA's short-range forecasts of precipitation and lower tropospheric atmospheric conditions over Singapore over the meteorological year December 2018 to November 2019, benchmarked against the European Centre for Medium-Range Weather Forecasts (ECMWF) High Resolution (HRES) global model. We found that SINGV-DA's performance varied between seasons, and that this seasonal variation is partly attributable to the driving model. Compared to the global model, which has a tendency to over-(under-) forecast light (heavy) rain events, SINGV-DA's precipitation forecasts are markedly more realistic.

## 1 INTRODUCTION

The Maritime Continent, situated in the tropics between the Indian and Pacific Oceans, is made up of thousands of islands separated by shallow seas. The meteorology of this region is dominated by diurnal cycles of convective activity driven by warm sea and land surface temperatures. Complex land-sea interactions coupled with weak synoptic forcings make short-range forecasts of such convective activity particularly difficult. Based on the few studies looking specifically at the performance of numerical weather prediction (NWP) systems over the Maritime Continent (McBride and Ebert, 2000; Hayashi, Aranami and Saito, 2008), it is quite clear that regional as well as global operational models are less skilful in short-range forecasts over the Maritime Continent than over mid-latitude regions.

To improve weather forecasts for the western part of the Maritime Continent (roughly centred over Singapore), Meteorological Service Singapore (MSS) collaborated with the Met Office to develop SINGV, a convective-scale

NWP system for the deep Tropics (Huang et al., 2019). Deterministic forecasts are provided by SINGV-DA (Heng et al., 2020), which couples the SINGV forecast model with a regional data assimilation system. Officially, SINGV-DA was put into operations in July 2019, but we have real-time forecast runs from a stable release version of SINGV-DA dating back to May 2018. Building on the work of Sun et al. (2020), who evaluated the skill of an earlier version of SINGV (without regional data assimilation) in forecasting Sumatra squalls, this paper examines the operational SINGV-DA's forecast performance over Singapore over four seasons in the meteorological year December 2018 to November 2019. The European Centre for Medium-Range Weather Forecasts (ECMWF) High Resolution (HRES) global model, which provides the lateral boundary conditions (LBCs) for SINGV-DA, is evaluated against the same set of observations to serve as a performance benchmark for the regional system.

The rest of this paper is organised as follows. The methodology is given in Section 2, wherein we describe the SINGV-DA system, the data used for verification, and the verification metrics adopted for model evaluation. The verification results are presented in Section 3. We conclude in Section 4 with a discussion of our findings and recommendations for further work.

## 2 METHODOLOGY

Following a brief description of the SINGV-DA system, this section describes the forecast data extracted, and the verification metrics adopted for model evaluation. The same methodology is applied to forecasts from ECMWF to allow for comparisons between the two models.

### 2.1 SINGV-DA

The SINGV-DA model domain is shown in Figure 1. The forecast model (Huang et al., 2019) runs on a regular longitude-latitude horizontal grid with a resolution of  $0.0135^\circ$  (approximately 1.5 km). There are 80 model levels in the vertical reaching up to 38.5 km.

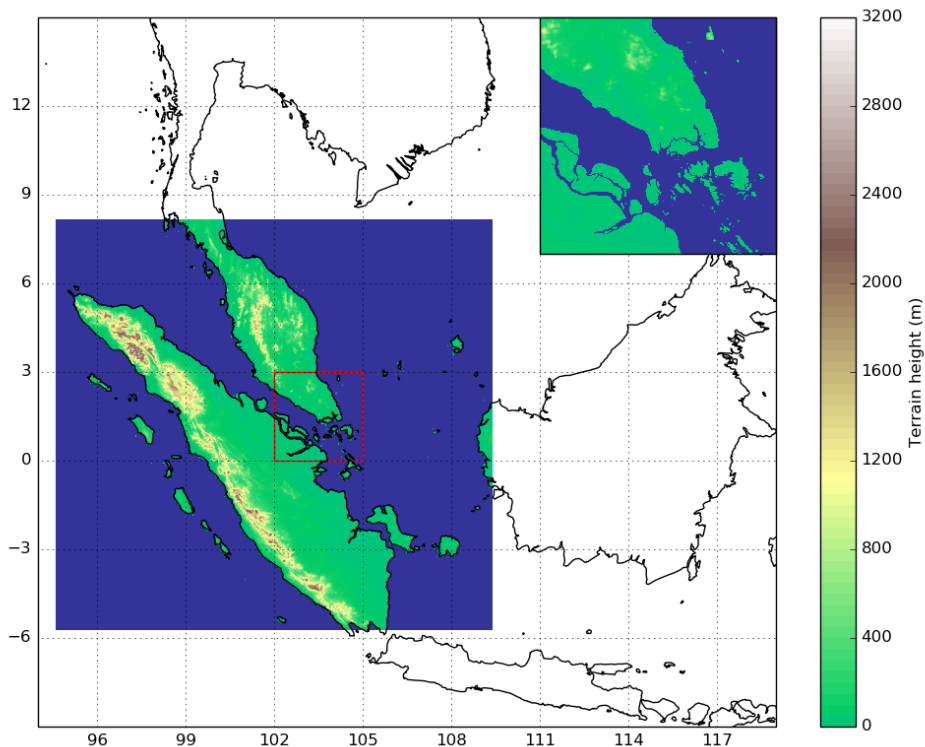


**Figure 1: The SINGV-DA domain, with model orography shaded and a zoomed-in view of the area around Singapore in the inset.**

The best-estimate initial conditions for each forecast cycle are produced by the regional data assimilation system using a three-dimensional variational (3D-Var) approach (Heng et al., 2020). This is done every three hours with an observation window of  $\pm 90$  minutes. The data currently assimilated include conventional observations, satellite radiances, scatterometer winds and, based on imagery from the geostationary Himawari-8 satellite, atmospheric motion vectors and pseudo cloud observations at the cloud top (Renshaw and Francis, 2011).

The forecast model is driven through its lateral boundaries by the ECMWF HRES model. The lateral boundaries are updated whenever a new ECMWF forecast cycle becomes available, such that the 03 (15) UTC cycle of SINGV-DA is driven by the 00 (12) UTC cycle of the ECMWF global model. Thus, we focus on verifying the 03 and 15 UTC cycles of SINGV-DA, benchmarked against the global model's 00 and 12 UTC cycles respectively.

## 2.2 Data

To verify model forecasts of atmospheric conditions over Singapore, we use the high-quality rawinsonde observations collected twice daily by the MSS Upper Air Observatory, which was recently certified as a Global Climate Observing System (GCOS) Reference Upper-Air

Network (GRUAN) site. For comparison with the rawinsonde observations, the model forecasts are interpolated to the location of the Upper Air Observatory. Within the boundaries of Singapore, lower tropospheric atmospheric conditions account for most of the weather phenomena of interest. As such, upper-air forecast verification in this work is restricted to the pressure levels 925, 850 and 700 hPa.

For precipitation over Singapore, we have data from MSS's dense network of rain gauges on the island (Figure 2). The observations and SINGV-DA's precipitation forecasts are accumulated over three-hourly periods to match the temporal resolution of ECMWF forecasts. The relatively coarse horizontal resolution of ECMWF forecasts does not permit point-based verification. Instead, the three-hourly rainfall forecasts are averaged over land points representing Singapore in the respective models (Figure 2) for verification against the observations averaged over rain gauges.

Table 1 shows the valid times at which the forecasts are verified against upper-air and rainfall observations and the corresponding forecast lead times with respect to the model cycles. We discard precipitation forecasts from the first nine (twelve) hours of each SINGV-DA (ECMWF) cycle because, based on the current operational forecasting schedule, these forecasts are not operationally useful.

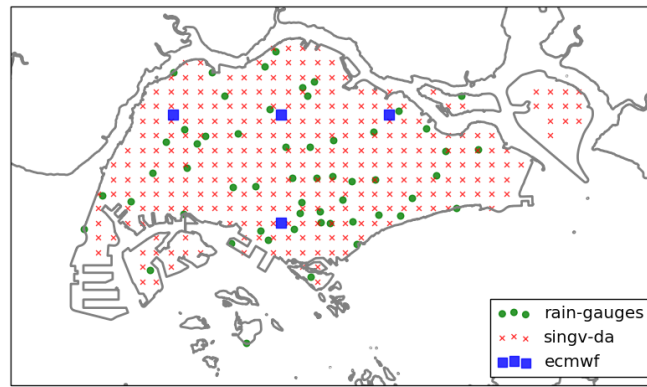


**Figure 2: Coastal outline of Singapore showing the locations of the rain gauges and the model land points representing Singapore for the purpose of verifying rainfall forecasts.**

Observations	Upper-air		Rainfall							
	00	12	00	03	06	09	12	15	18	21
ECMWF (00)	T+24	-	T+24	T+27	T+30	T+33	T+36	T+15	T+18	T+21
SINGV-DA (03)	T+21	-	T+21	T+24	T+27	T+30	T+33	T+12	T+15	T+18
ECMWF (12)	-	T+24	T+36	T+15	T+18	T+21	T+24	T+27	T+30	T+33
SINGV-DA (15)	-	T+21	T+33	T+12	T+15	T+18	T+21	T+24	T+27	T+30

**Table 1: Observation valid times and the corresponding forecast lead times with respect to the model cycles.**

### 2.3 Verification Metrics

For upper-air variables (relative humidity, temperature and winds), we use mean biases and root-mean-square errors (RMSEs) to evaluate forecast performance. These give us, for each model, for each variable, at each pressure level, a pair of statistics quantifying forecast deviations from observations.

For rainfall over Singapore, we construct a contingency table, the format of which is shown in Table 2, for each of six three-hourly rainfall thresholds: 0.1, 0.2, 0.5, 1, 2 and 5 mm. With two cycles per model (Table 1), we have a total of 12 contingency tables per model.

		Observed		Total
		Yes	No	
Forecast	Yes	A	B	A + B
	No	C	D	C + D
Total		A + C	B + D	A + B + C + D

**Table 2: Generic contingency table format, showing hits (A), false alarms (B), misses (C) and correct negatives (D).**

The following statistics are derived from each contingency table:

$$\text{Probability of detection (POD)} = \frac{A}{A + C}$$

$$\text{False alarm ratio (FAR)} = \frac{B}{A + B}$$

$$\begin{aligned} \text{Threat score or critical success index (CSI)} \\ = \frac{A}{A + B + C} \end{aligned}$$

$$\text{Frequency bias} = \frac{A + B}{A + C}$$

To facilitate comparisons, these statistics are represented as a point on a performance diagram with the coordinates (SR, POD), where SR = 1 – FAR is the success ratio (Roebber, 2009). A perfect forecasting system with POD = 1, FAR = 0, CSI = 1 and bias = 1 would therefore be represented as a point on the top right corner of the performance diagram.

The verification statistics were calculated for each of the four seasons in Singapore—northeast monsoon (December – March), first inter-monsoon (April – May), southwest monsoon (June – September) and second inter-monsoon (October – November)—in the meteorological year December 2018 to November 2019.

### 3 RESULTS

#### 3.1 Upper-Air Variables

The mean biases and RMSEs in upper-air relative humidity (RH) and temperature forecasts over Singapore at T+24 for ECMWF and T+21 for SINGV-DA are shown in Figure 3. At 925 hPa, SINGV-DA forecasts of RH and temperature were generally better than the global model's. This is most evident during the inter-monsoon periods (April – May and October – November), where

we see large reductions in RH and temperature biases due to downscaling.

On the other hand, there appears to be a systematic dry bias in SINGV-DA forecasts at 850 hPa that cannot be attributed to the driving model. This bias in RH reflects the warm bias, relative to the global model as well as observations, that we see in SINGV-DA forecasts at 850 hPa. The diagnostic plots for October 2019 (Figure 4) clearly illustrate this, as large dry biases at 850 hPa generally coincide with large warm biases.

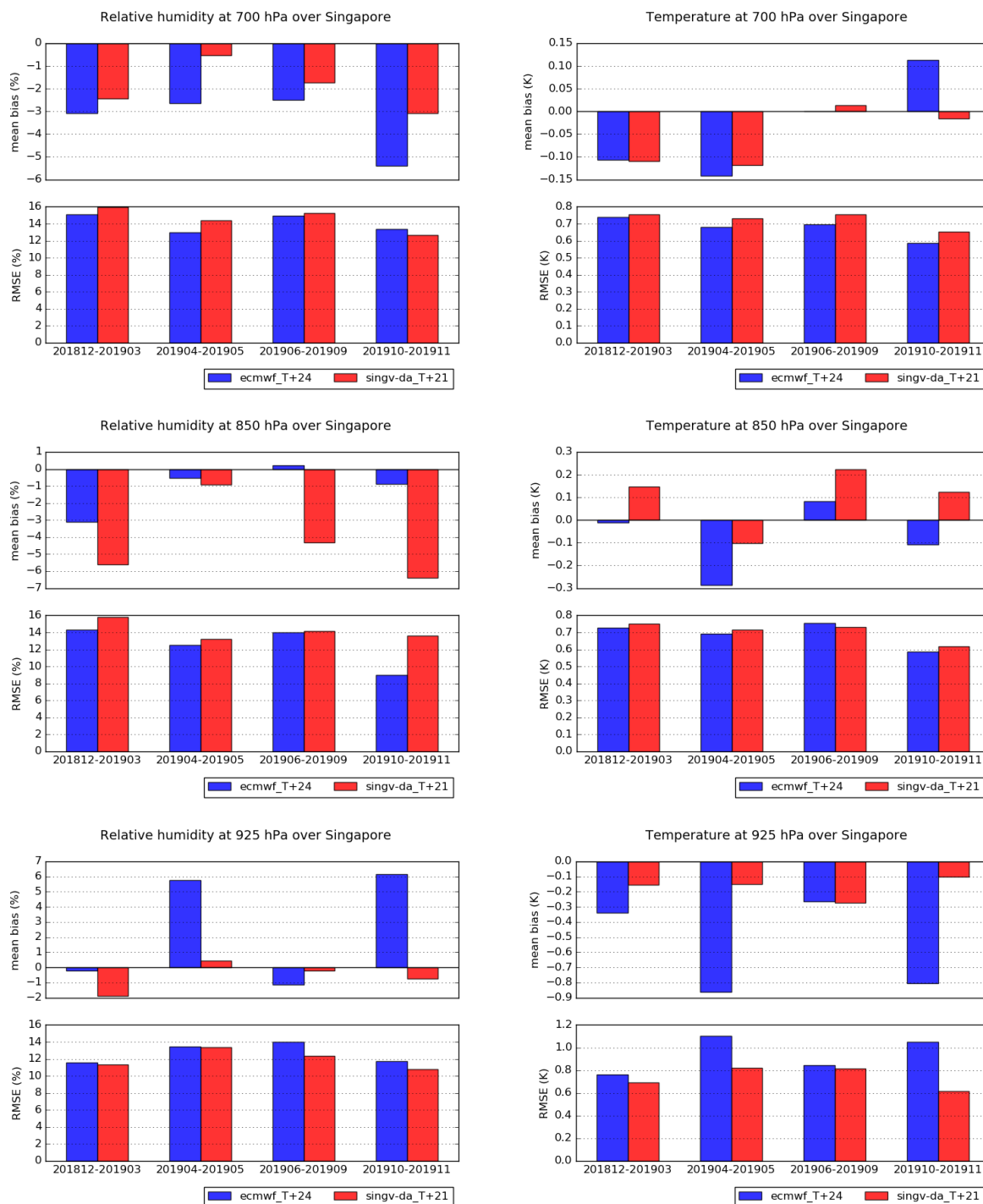
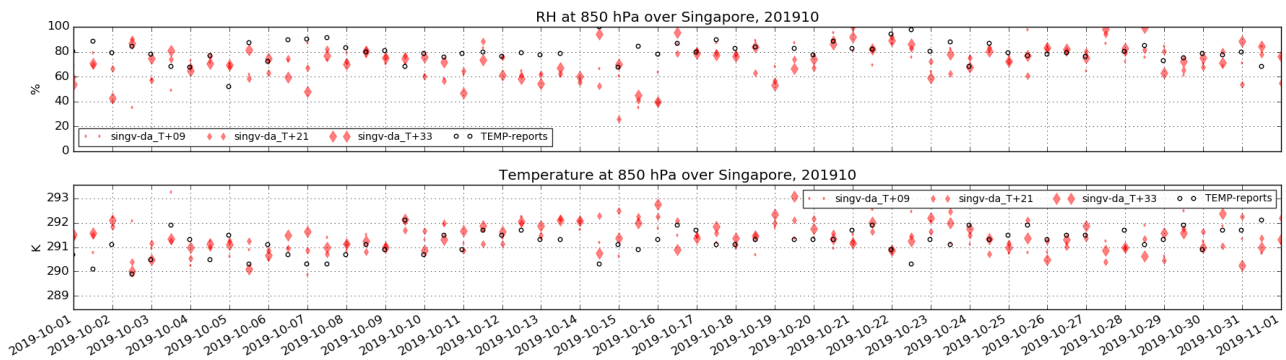


Figure 3: Seasonal mean biases and RMSEs in relative humidity (left) and temperature (right) forecasts over Singapore at T+24 for ECMWF and T+21 for SINGV-DA at 700 (upper), 850 (middle) and 925 hPa (lower).



**Figure 4: SINGV-DA forecasts of RH (top) and temperature (bottom) at 850 hPa compared to rawinsonde observations in October 2019.**

The errors in SINGV-DA forecasts of RH and temperature at 700 hPa are generally in line with global model errors.

The mean biases and RMSEs in the wind forecasts over Singapore are shown in Figure 5. There appears to be a systematic bias across seasons in the meridional component of ECMWF wind forecasts at 700 hPa. This bias was especially large in the first inter-monsoon period (April – May), during which the mean winds in both models had a southerly (positive meridional) component, as opposed to the observations.

At the 925 hPa level, SINGV-DA winds appear to have a systematically stronger easterly (negative zonal) component than the observed winds. This bias cannot be attributed to the global driving model since the ECMWF forecasts had, in all but one season, mean biases in the opposite direction. On the other hand, the easterly biases in SINGV-DA at 925 hPa are smaller than the westerly biases in the global model during the inter-monsoon periods (April – May and October – November).

Since RMSEs tend to increase with the variability of the observations (Koh and Ng, 2009), a convenient gauge of forecast performance across seasons is the magnitude of the RMSE relative to the standard deviation of the observations. We observe that, in general, the RMSEs in the wind forecasts were smaller than the standard deviations of the observations (Figure 5), with the only exception occurring during the southwest monsoon season (June – September) in the zonal component of SINGV-DA wind forecasts at 925 hPa.

### 3.2 Precipitation

The contingency table statistics are plotted on the performance diagrams shown in Figure 6, with each point representing the average of two cycles (per model) and the horizontal and vertical ‘error’ bars showing the range of the SR and POD respectively for a specified

rainfall threshold. The ‘error’ bars are as such surrogates for the uncertainties associated with the metrics, which in this case arise from the model cycles being initialised at different times.

The performance diagrams show that, in general, threat scores (CSI) are lower for the rarer heavy rain events. For a target score of CSI = 0.2, generally only events smaller than 1 mm in 3 hours (averaged over the Singapore land area) may be forecast with sufficient skill.

We may also observe that, consistently across the seasons, SINGV-DA and ECMWF rainfall forecasts have markedly different characteristics. The global model tends to over-(under-)forecast light (heavy) precipitation events, whereas SINGV-DA is significantly less biased, with the points lining up close to the diagonal in Figure 6.

There are clear seasonal variations in model performance. SINGV-DA performed poorly during the southwest monsoon season (June – September) and significantly better during the northeast monsoon season (December – March). This was also true for the global model, demonstrating the connection between SINGV-DA’s performance and that of its driving model.

There appears to be no correlation between these statistics and model errors in lower tropospheric temperature and moisture (Figure 3). To illustrate, the ECMWF precipitation forecasts during the inter-monsoon periods were not discernibly poorer even though contemporaneous forecasts of temperature at 925 hPa suffered from relatively large mean biases and RMSEs. Similarly, relatively small (large) mean biases in SINGV-DA forecasts of RH at 850 hPa in the first (second) inter-monsoon period are not associated with more (less) skilful precipitation forecasts.

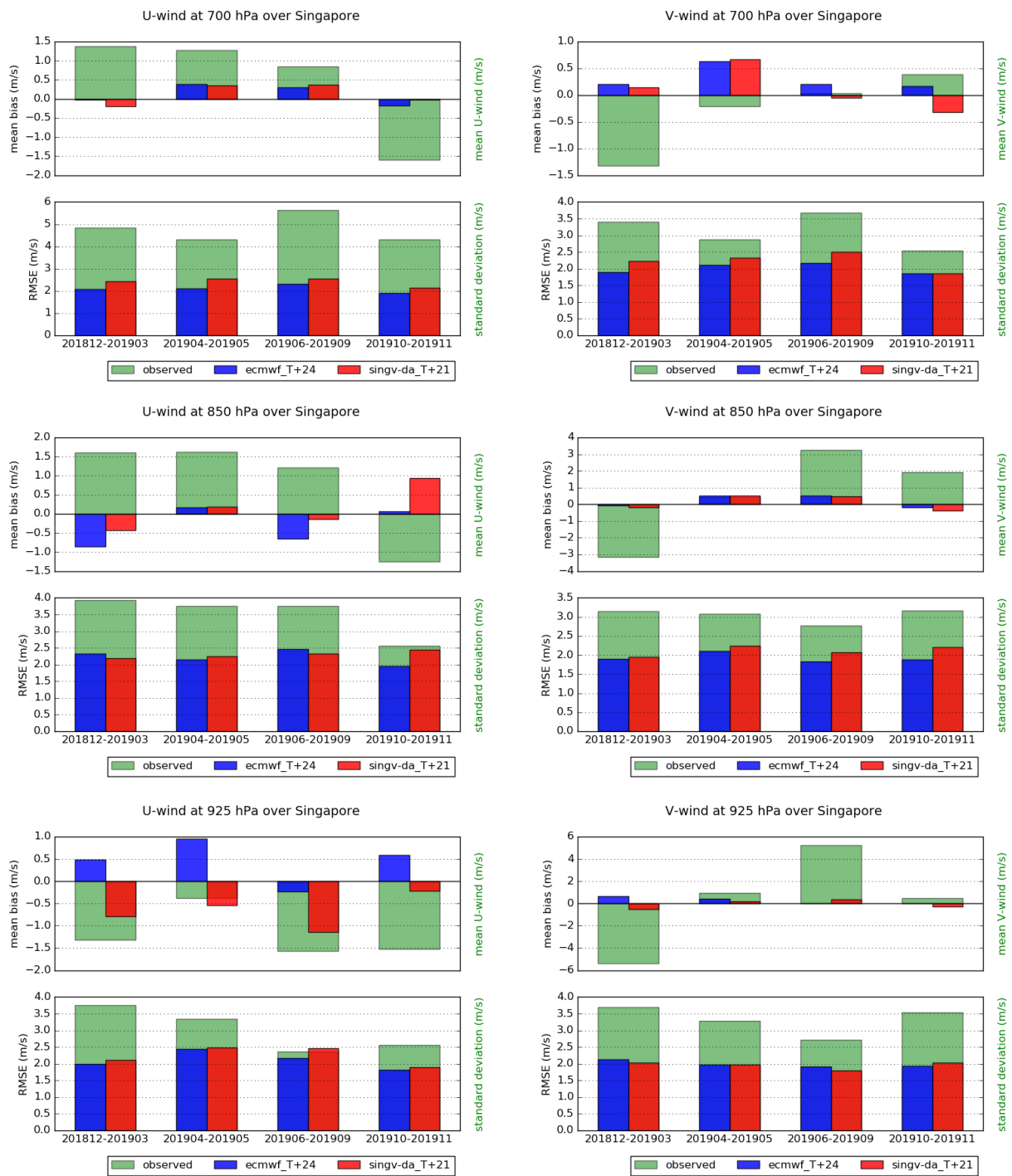


**Figure 5: Seasonal mean biases and RMSEs in the zonal (left) and meridional (right) components of wind forecasts over Singapore at T+24 for ECMWF and T+21 for SINGV-DA at 700 (upper), 850 (middle) and 925 hPa (lower). The observed mean wind components and standard deviations are also plotted to provide perspective.**

Instead, there appears to be a link, for the global model as well as SINGV-DA, between rainfall forecast skill and errors in the zonal wind component at 925 hPa (Figure 5). In particular, the poor precipitation forecasts in SINGV-DA during the southwest monsoon season are associated with relatively large errors in the zonal wind component at 925 hPa in the same period.

## 4 DISCUSSION AND CONCLUSIONS

We have presented in this work the first full-year objective evaluation of SINGV-DA and ECMWF deterministic forecasts over Singapore. While the performance metrics are far from being comprehensive, they do provide an important first look at the characteristics of short-range forecasts of significant variables in this region. We summarise our main findings

in this concluding section with recommendations for further research.

It is clear from the results that model forecast performance varies from season to season. The roughly synchronous variations in the performance of the models demonstrate the coupling between SINGV-DA and its driving model, which underscores the importance of the LBCs even for a limited area model in the tropics, where the synoptic atmospheric forcing is relatively

weak. On the other hand, SINGV-DA is not a mere slave of its driving model, since the difference in skill between the models also varies from season to season (see, for example, Figure 3). We may therefore conclude that SINGV-DA exhibits a degree of dependence on its driving model but modifies the global forecast for better or for worse according to its strengths and weaknesses in capturing meteorological phenomena in this region.

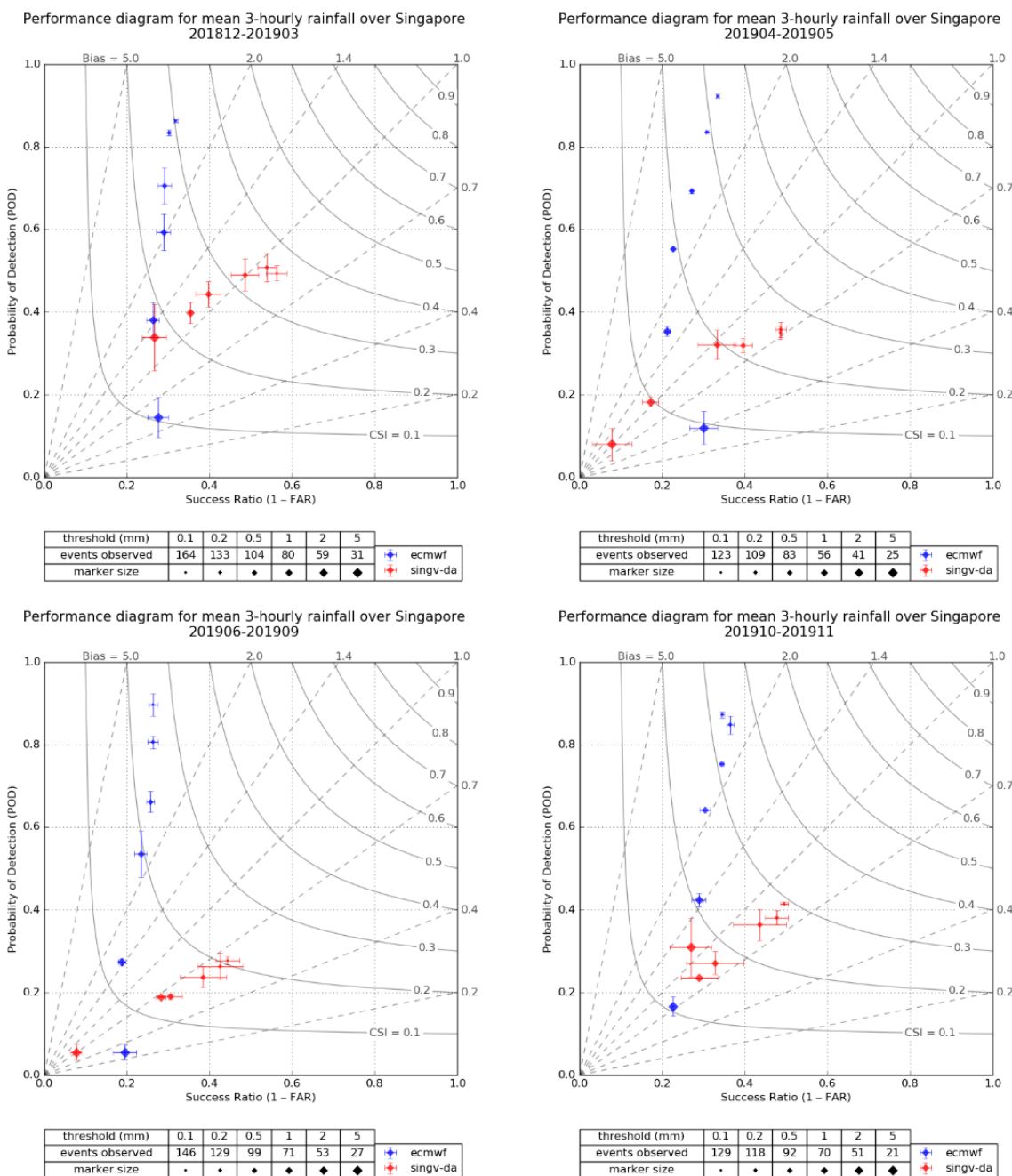


Figure 6: Seasonal performance diagrams for rainfall over Singapore. Each point represents the contingency table metrics for a specified rainfall threshold (shown in the tables below) averaged over two cycles per model. The SR and POD are given by the x- and y-coordinates, while the frequency bias and CSI are represented by the position of the point with respect to the diagonal dashed lines and the solid contours respectively. The table also shows the number of observed events exceeding each threshold.

We also see in the seasonal variations in performance statistics a tentative link between low-level winds and precipitation over Singapore. In contrast, there is little correlation between errors in the lower tropospheric thermodynamic variables and precipitation forecast skill.

The performance statistics presented in this work show that SINGV-DA forecasts of lower tropospheric atmospheric conditions are generally on par with those of the world-leading ECMWF global model (Section 3.1). We see added value in SINGV-DA forecasts at 925 hPa, particularly during the inter-monsoon periods, which are characterised by weak and variable winds. This underscores the benefit of a high-resolution representation of the topography of the Maritime Continent, which exerts a strong influence on near-surface atmospheric conditions in the absence of strong synoptic drivers.

The rainfall forecast statistics (Figure 6) highlight the fundamental difference between the global model and SINGV-DA in representing convective processes. SINGV-DA forecasts are clearly more realistic (in terms of frequency bias) across the full range of rainfall thresholds examined in this work. This is consistent with climate modelling studies in the past showing the limitations of global models with parametrised convection (Neale and Slingo, 2003; King and Vincent, 2018) and the benefits of convection-permitting simulations over the Maritime Continent (Love, Matthews and Lister, 2011; Holloway, Woolnough and Lister, 2012; Vincent and Lane, 2017; Argüeso, Romero and Homar, 2020).

While SINGV-DA's threat scores for heavy rain events over Singapore are not consistently higher than the global model's, this should be interpreted in light of the small spatial scale of evaluation, the total land area of Singapore being just over 720 km<sup>2</sup>. We can expect to see more added value in SINGV-DA forecasts of precipitation at larger scales (Clark et al., 2016).

The verification statistics presented in this work should feed back into model development to improve SINGV. The seasonal variations in SINGV-DA's performance suggest that the model performs better in some weather regimes than others. Further work to stratify the verification statistics by weather regimes such as those identified by Hassim and Timbal (2019) would be needed to isolate model flaws. This would complement the work of Sun et al. (2020), who evaluated the SINGV's forecast skill specifically in relation to Sumatra squalls.

Based on the apparent link between low-level wind forecast errors and precipitation forecast skill, and evidence in the literature that low-level convergence plays an important role in thunderstorm initiation in this region (Weller et al., 2017), we may hypothesise that improving low-level wind forecasts in SINGV-DA would be crucial to obtaining better precipitation forecasts. This could be achieved through improving the convective-scale data assimilation system (Gustafsson et al., 2018; Heng et al., 2020) or by using the global forecast to nudge SINGV-DA dynamical fields in the interior of the domain (Zhao et al., 2016).

On the other hand, we should not dismiss the possibility that forecast errors in the low-level winds are symptomatic—rather than the cause—of poor precipitation forecasts, as strong updraughts in deep convection and the subsequent downdraughts in precipitating cores may modify low-level winds. From this perspective, gains in forecast performance may be obtained by improving the representation of precipitation processes in SINGV-DA.

Finally, we may gain further insights by verifying the forecasts against observations with higher resolutions in space and time, such as surface observations and radar data. Similarly, the use of other verification metrics such as the Stable Equitable Error in Probability Space (Rodwell et al., 2010) and methods such as Structure-Amplitude-Location (Wernli et al., 2008) may help to clarify model tendencies.

## 5 ACKNOWLEDGMENTS

The contributions of Xiangming Sun, who led early efforts at MSS in model evaluation, are gratefully acknowledged. We thank Wee Kiong Cheong and other operational meteorologists at MSS for their feedback in the selection of verification metrics. Credit goes also to Jeff Lo and Jerry Liu for the operational implementation and maintenance of SINGV-DA.

## 6 REFERENCES

- Argüeso, D., Romero, R. and Homar, V. (2020) 'Precipitation Features of the Maritime Continent in Parameterized and Explicit Convection Models', *Journal of Climate*, vol. 33, no. 6, pp. 2449-2466.
- Clark, P., Roberts, N., Lean, H., Ballard, S.P. and Charlton-Perez, C. (2016) 'Convection-permitting models: a step-change in rainfall forecasting', *Meteorological Applications*, vol. 23, pp. 165-181.

- Gustafsson, N., Janjić, T., Schraff, C., Leuenberger, D., Weissmann, M., Reich, H., Brousseau, P., Montmerle, T., Wattrelot, E., Bučánek, A., Mile, M., Hamdi, R., Lindskog, M., Barkmeijer, J., Dahlbom, M., Macpherson, B., Ballard, S., Inverarity, G., Carley, J., Alexander, C., Dowell, D., Liu, S., Ikuta, Y. and Fujita, T. (2018) 'Survey of data assimilation methods for convective-scale numerical weather prediction at operational centres', *Quarterly Journal of the Royal Meteorological Society*, vol. 144, pp. 1218-1256.
- Hassim, M.E.E. and Timbal, B. (2019) 'Observed Rainfall Trends over Singapore and the Maritime Continent from the Perspective of Regional-Scale Weather Regimes', *Journal of Applied Meteorology and Climatology*, vol. 58, no. 2, pp. 365-384.
- Hayashi, S., Aranami, K. and Saito, K. (2008) 'Statistical Verification of Short Term NWP by NHM and WRF-ARW with 20 km Horizontal Resolution around Japan and Southeast Asia', *Scientific Online Letters on the Atmosphere*, vol. 4, pp. 133-136.
- Heng, B.C.P., Tubbs, R., Huang, X.-Y., Macpherson, B., Barker, D.M., Boyd, D.F.A., Kelly, G., North, R., Stewart, L., Webster, S. and Wlasak, M. (2020) 'SINGV-DA: A data assimilation system for convective-scale numerical weather prediction over Singapore', *Quarterly Journal of the Royal Meteorological Society*, pp. 1-16.
- Holloway, C.E., Woolnough, S.J. and Lister, G.M.S. (2012) 'Precipitation distributions for explicit versus parametrized convection in a large-domain high-resolution tropical case study', *Quarterly Journal of the Royal Meteorological Society*, vol. 138, no. 668, pp. 1692-1708.
- Huang, X.-Y., Barker, D., Webster, S., Dipankar, A., Lock, A., Mittermaier, M., Sun, X., North, R., Darvell, R., Boyd, D., Lo, J., Liu, J., Macpherson, B., Heng, P., Maycock, A., Pitcher, L., Tubbs, B., McMillan, M., Zhang, S., Hagelin, S., Porson, A., Song, G., Beckett, B., Cheong, W.K., Semple, A. and Gordon, C. (2019) 'SINGV – the Convective-Scale Numerical Weather Prediction System for Singapore', *ASEAN Journal on Science & Technology for Development*, vol. 36, no. 3, pp. 81-90.
- King, A.D. and Vincent, C.L. (2018) 'Using Global and Regional Model Simulations to Understand Maritime Continent Wet-Season Rainfall Variability', *Geophysical Research Letters*, vol. 45, no. 22, pp. 12534-12543.
- Koh, T.-Y. and Ng, J.S. (2009) 'Improved diagnostics for NWP verification in the tropics', *Journal of Geophysical Research*, vol. 114, p. D12102.
- Love, B.S., Matthews, A.J. and Lister, G.M.S. (2011) 'The diurnal cycle of precipitation over the Maritime Continent in a high-resolution atmospheric model', *Quarterly Journal of the Royal Meteorological Society*, vol. 137, no. 657, pp. 934-947.
- McBride, J.L. and Ebert, E.E. (2000) 'Verification of Quantitative Precipitation Forecasts from Operational Numerical Weather Prediction Models over Australia', *Weather and Forecasting*, vol. 15, pp. 103-121.
- Neale, R. and Slingo, J. (2003) 'The Maritime Continent and Its Role in the Global Climate: A GCM Study', *Journal of Climate*, vol. 16, no. 5, pp. 834-848.
- Renshaw, R. and Francis, P.N. (2011) 'Variational assimilation of cloud fraction in the operational Met Office Unified Model', *Quarterly Journal of the Royal Meteorological Society*, vol. 137, pp. 1963-1974.
- Rodwell, M.J., Richardson, D.S., Hewson, T.D. and Haiden, T. (2010) 'A new equitable score suitable for verifying precipitation in numerical weather prediction', *Quarterly Journal of the Royal Meteorological Society*, vol. 136, no. 650, pp. 1344-1363.
- Roebber, P.J. (2009) 'Visualizing Multiple Measures of Forecast Quality', *Weather and Forecasting*, vol. 24, no. 2, pp. 601-608.
- Sun, X., Huang, X.-Y., Gordon, C., Mittermaier, M., Beckett, R., Cheong, W.K., Barker, D., North, R. and Semple, A. (2020) 'A Subjective and Objective Evaluation of Model Forecasts of Sumatra Squall Events', *Weather and Forecasting*, vol. 35, no. 2, pp. 489-506.
- Vincent, C.L. and Lane, T.P. (2017) 'A 10-Year Austral Summer Climatology of Observed and Modeled Intraseasonal, Mesoscale, and Diurnal Variations over the Maritime Continent', *Journal of Climate*, vol. 30, no. 10, pp. 3807-3828.
- Weller, E., Shelton, K., Reeder, M.J. and Jakob, C. (2017) 'Precipitation associated with convergence lines', *Journal of Climate*, vol. 30, pp. 3169-3183.
- Wernli, H., Paulat, M., Hagen, M. and Frei, C. (2008) 'SAL—A Novel Quality Measure for the Verification of Quantitative Precipitation Forecasts', *Monthly Weather Review*, vol. 136, no. 11, pp. 4470-4487.

Zhao, Y., Wang, D., Liang, Z. and Xu, J. (2016) 'Improving numerical experiments on persistent severe rainfall events in southern China using spectral nudging and filtering schemes', *Quarterly Journal of the Royal Meteorological Society*, vol. 142, no. 701, pp. 3115-3127.

# Preliminary evaluation of the *NOAA-20/JPSS-1 Active Fires 750m* satellite product in Sumatra and Borneo using Sentinel-2 satellite data

Efthymia Pavlidou, Songhan Wong

Weather Services Department, Meteorological Service Singapore

## ABSTRACT

Timely detection and monitoring of active forest and land fires are crucial and challenging for Southeast Asia, considering the ecosystem complexity and the severity of fire and smoke haze impacts in the region. Global satellite-based products are operationally available but need to be assessed, and potentially adjusted, to address local conditions. In this study, hotspots detected by the *NOAA-20/JPSS-1 Active Fires* operational product suite are verified in wet and dry months (January and July 2019) in fire prone areas of Sumatra and Borneo in Southeast Asia. Given the scarcity of ground-based data, verification is based on high spatial resolution optical imagery from Sentinel-2 allowing for detailed visual examination of the study areas. Furthermore, Fire Radiative Power (FRP) estimates from the *NOAA-20/JPSS-1 Active Fires* product suite are examined along with the Confidence Levels reported for the detections. High Precision scores are found overall ( $> 0.70$ ) indicating that the majority of reported hotspots in *NOAA-20/JPSS-1 Active Fires* corresponded to actual fires seen in Sentinel-2. However, the number of missed detections was almost as high as the number of reported hotspots. Common reasons for missed detections are cloud cover and the presence of smoke obscuring burning areas. When higher Confidence Levels of reported hotspots are considered, hotspot detection performance improves. At the same time, high Confidence Levels coincide already with fires of low estimated FRP, indicating a potential for early fire detection. Finally, the study demonstrates an approach to quantitatively consider Confidence Levels in order to optimise utilisation of the product for decision-making.

## 1 INTRODUCTION

Forest and land fire occurrence and intensity are reportedly increasing worldwide, with catastrophic effects on ecosystem loss, greenhouse gas emissions and poor air quality (Liu and Stanturf, 2010). These trends are particularly relevant in Southeast Asia, where transboundary haze pollution arising from forest and land fires has resulted in significant impact to the economy, public health and environment. Satellite-based fire detection plays a crucial role in helping local authorities prioritise their limited resources and undertake mitigation measures effectively, especially in remote areas that lack ground-based data.

The Meteorological Service Singapore (MSS)<sup>1</sup> utilises satellite data from a wide range of geostationary and polar-orbiting sensors on board satellites including NOAA-20, Suomi-NPP, TERRA, AQUA, METOP, Sentinel, Himawari-8 and FY-4A (for further information on meteorological satellites see (Schmetz and Menzel, 2015) and the references therein). Among the latest operationally available products is the *NOAA-20/JPSS-1 Active Fires* product which provides active fire pixels and associated detection confidence estimates, along with Fire Radiative Power (FRP) calculations, which is a measure of the radiant energy released per unit time. Active fire detection is based on multi-spectral observations of the Visible Infrared Imaging Radiometer Suite sensor (VIIRS) on board the NOAA-20 polar orbiting satellite. The sensor's sampling and radiometric features are well-suited for operational fire monitoring (Csiszar et al., 2013), during day and night time using separate algorithms respectively. In the latest version, the detection algorithms apply a sequence of adjusted threshold-based and contextual tests to flag hotspots and subsequently reject false positives, with the

---

<sup>1</sup> MSS hosts the ASEAN Specialized Meteorological Centre whose responsibility is to monitor, assess and provide early warnings of the occurrence of

transboundary haze from land and forest fires in the region.

intention to improve detection capability as compared to previous versions of the product (Schroeder et al., 2014).

Preliminary assessments of the algorithm on the global scale have shown improvements in detection rates and reduction in false positives (Schroeder et al., 2014; Csiszar et al., 2013). However, product evaluations till now rely on a limited number of test case studies using ground- and airborne-fire data, as well as on inter-comparisons with previous versions of the same product (Csiszar et al., 2018). The product provider further notes that the algorithm is tuned to minimise errors globally, and that its performance is expected to vary locally. This has to be taken into consideration for Southeast Asia because the complexity of biomass burning in the region (Reid et al., 2013) makes the task of monitoring even more challenging. In order to quantify the product's limitations and optimise its use in our region, verification of the product was conducted in selected fire-prone locations in Southeast Asia.

This report shares preliminary verification results of the hotspots detected by the NOAA-20/JPSS-1 Active Fires satellite product on the islands of Sumatra and Borneo in January (wet season) and July (dry season) 2019. Given the lack of ground-based datasets, high-resolution images from the Sentinel-2 optical satellite were used to verify reported hotspots and identify missed detections (Filipponi, 2019). Sentinel-2 imagery, due to its high

spatial resolution, has shown great potential and has been used for applications ranging from mangrove tree mapping, sub-pixel landscape feature characterisation and ship recognition, to burnt area detection and active fire monitoring (Atzberger, 2016; Roteta et al., 2019; Cicala et al., 2018; Amos et al., 2019). Confidence Levels and Fire Radiative Power estimates were examined to understand the performance of the detection algorithm.

## 2 DATA AND METHODS

### 2.1 Data

NOAA-20 hotspots were retrieved from MSS' archives, and Sentinel-2 imagery was acquired through the Copernicus Open Access Hub (<https://scihub.copernicus.eu>). Sentinel-2 imagery was chosen due to its high spatial resolution (10-60 m depending on the band) and high revisit frequency (5-day revisit time) as compared to other similar satellites. Fire-prone areas with varying nature of burning activities (from isolated fires to large clusters of fires) were chosen for analyses in the neighbourhood of Singapore – in central Sumatra and Borneo (Figure 1). Sentinel-2 image tiles for January and July 2019 were retrieved to collect samples that represent typical conditions in months with low and high levels of fire occurrence respectively. Tiles from months that would be completely covered by

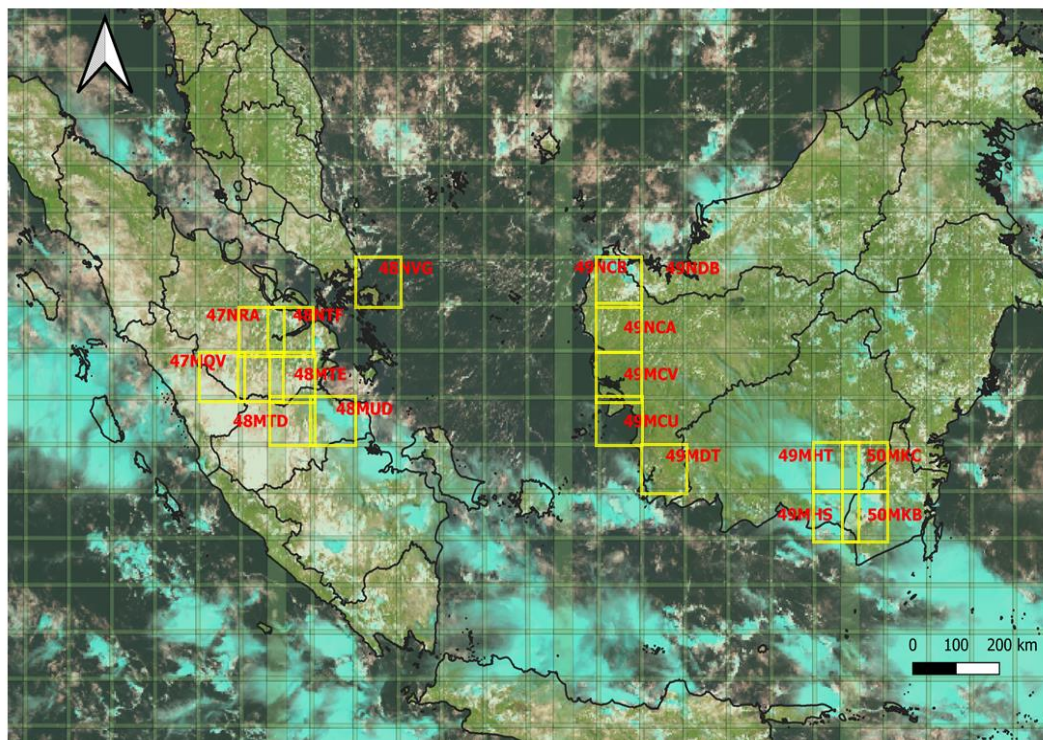


**Figure 1: Location of selected Sentinel-2 tiles over the studied areas (highlighted). Tile 48NVG to the east of Singapore is grouped with the Sumatra data subset. Underlying image: Himawari-8 RGB True colour composite.**

<b>True Positive</b>	<ul style="list-style-type: none"> <li>• A NOAA-20 hotspot coincides with an active fire visible on a Sentinel-2 image on the same and/or immediately preceding date and within the same 750 m grid cell (e.g. in Figure 2, examples are indicated as C1, C2 and C3). It would be reasonable to assume that two hotspots appearing in the same location within 24 hours correspond to a single fire rather than a second fire breaking out in an already burnt location.</li> <li>• A NOAA-20 hotspot is located within the same 750 m grid cell as a burned scar visible in the Sentinel-2 image of an immediately available subsequent date, where the burned scar is not visible at the same location in a Sentinel-2 image of the immediately available preceding date. For example, if a NOAA-20 hotspot is reported on July 20<sup>th</sup> and there is no available Sentinel image on that date, the hotspot is confirmed if a burned scar is present in the same location in an image on July 22<sup>nd</sup> and is not present in an image on July 18<sup>th</sup> (example as in label 'E' in Figure 2).</li> </ul>
<b>False Positive</b>	<ul style="list-style-type: none"> <li>• A hotspot is reported by NOAA-20 but there is no visible active fire in a Sentinel-2 image on the same and/or immediately preceding date and within the same 750 m grid cell.</li> <li>• A hotspot is reported by NOAA-20 but there is no burnt scar visible on the same or immediately subsequent available date on a Sentinel-2 image within the same 750 m grid cell.</li> </ul>
<b>Missed Detection (False Negative)</b>	<ul style="list-style-type: none"> <li>• Active fires are present in the Sentinel-2 image, but no NOAA-20 detection is reported in the same 750 m grid cell on the same date (example as in label 'A' in Figure 2).</li> <li>• Burnt scars are present in a Sentinel-2 image and are not present in the immediately preceding image, and no hotspot was detected in between. In that case, only one missed detection is registered, and it is assigned the date range between the two available images as it could have appeared at any time in between.</li> </ul>
<b>Not verifiable</b>	<ul style="list-style-type: none"> <li>• There is cloud cover on the location of a reported hotspot on the images on/close to the same date.</li> <li>• A hotspot is reported on the edge of the tile and there is no visible active fire or burned scar within the image.</li> </ul>

**Table 1: Criteria for hotspot verification**

extensive fires were not selected to avoid bias (Csiszar, et al., 2006). Extensive fires are easier to detect by the algorithms, but a timely response requires that fires need to be detected before they become extensive. We used information on the locations of flagged hotspots, associated confidence intervals and FRP for all hotspots within the chosen Sentinel-2 tiles. We then visually

inspected and analysed Sentinel imagery based on two Red-Green-Blue (RGB) colour composites: [SWIR@1.6](#)  $\mu\text{m}$ , [NIR@0.86](#)  $\mu\text{m}$ , and [VIS@0.66](#)  $\mu\text{m}$ ; and [NIR@0.86](#)  $\mu\text{m}$ , [VIS@0.66](#)  $\mu\text{m}$  and [VIS@0.56](#)  $\mu\text{m}$ . These RGB composites are designed to detect fire, smoke and burnt areas. All bands were sampled to a 20 m grid.

## 2.2 Verification procedure

Despite the suitability of Sentinel-2 for verification (high spatial resolution and revisit frequency), challenges exist. Firstly, the two sensors on board Sentinel-2 and NOAA-20 have different spatial resolutions (20 m for Sentinel-2 and 750 m for NOAA-20's VIIRS). Furthermore, the morning orbital overpass of Sentinel-2 does not coincide with NOAA's afternoon overpass; and Sentinel-2 (5-days) has a lower revisit frequency than NOAA-20 (1-day). To account for the difference in spatial resolution between the sensors, a 750 m-grid is overlaid

on the Sentinel-2 imagery and hotspots in the 750 m-grid are verified with the corresponding 20 m-grid cells where they are observed. To account for the temporal differences between the sensors, Sentinel-2 imagery is used to verify reported hotspots from NOAA-20 on the same day and in the time interval between acquisitions. The detailed verification criteria are presented in Table 1.

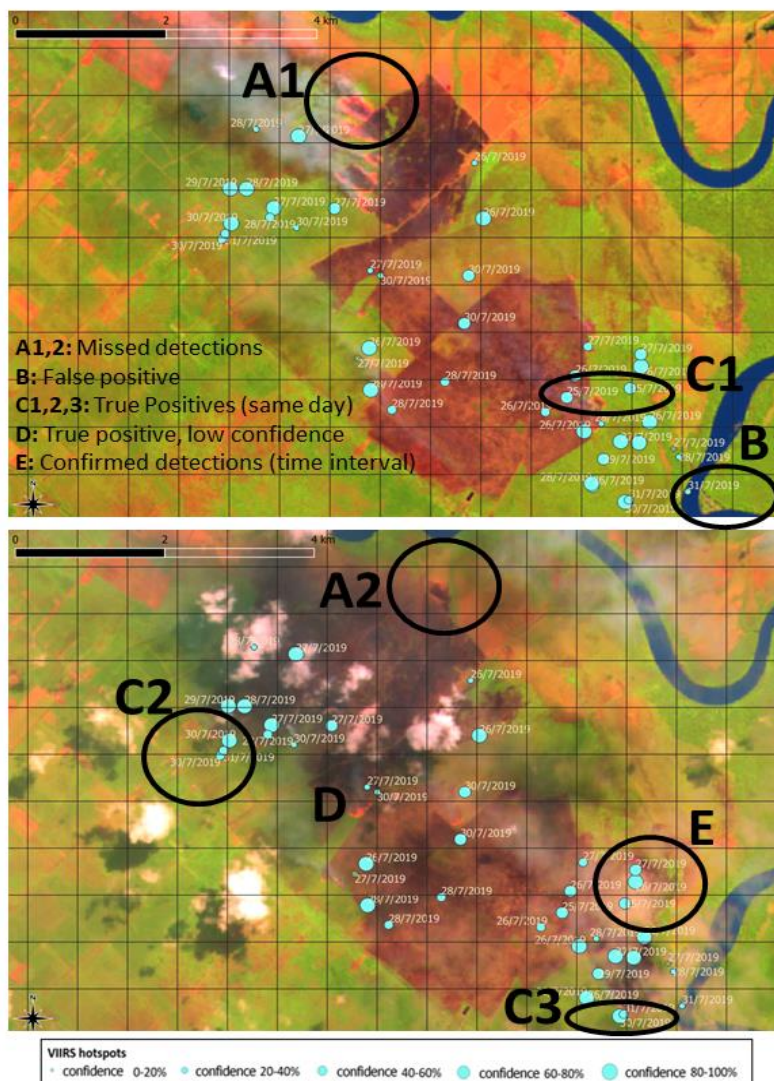


**Figure 2: Examples of NOAA-20 VIIRS hotspot verification (cyan circles; size scaled to confidence level) using Sentinel-2 imagery (background image). The grids are the 750 m grids of the NOAA-20 VIIRS. Detail from Borneo Tile T49MHT, 25/7/2019 (above) and 30/7/2019 (below). A1, 2: missed detections. No NOAA-20 hotspot is reported over fires detected on Sentinel-2 within the 750-m grid tile. B: False detection. Low confidence hotspot is reported in the river. C1, 2, 3: Confirmed same-date detections. There are active fires visible within 750m of the reported hotspots on the same date as the image. D: Same as (C), but the detected hotspot is assigned very low confidence despite the large active fire in the grid cell. E: Confirmed hotspots within a time interval. The reported hotspots (26/7/2019, 27/7/2019) appear in a location where there is a burnt scar in the subsequent available image (30/7/2019) and there is no burnt scar in the preceding image (25/7/2019).**

Metric	Interpretation	Formula
<b>Precision</b>	Ratio of the reported detections that were actual fires. Perfect score is 1.0	$Precision = \frac{TP}{TP + FP}$
<b>Recall</b>	Ratio of all the actual fires which were correctly detected. Perfect score is 1.0	$Recall = \frac{TP}{TP + FN}$
<b>F1-score</b>	Weighted average of Precision and Recall indicating overall detection performance. Ideal F1 score=1	$F1 = \frac{2(Precision * Recall)}{Precision + Recall}$
<b>Area Under the Curve (AUC)</b>	An expression of the potential to optimise the trade-off between Precision and Recall by considering different detection confidence thresholds	The area under a precision/recall curve

**Table 2: Performance metrics applied to evaluate hotspot detection**

Small fires covering an area less than 5x5 Sentinel-2 pixels (100x100 m) were excluded from verification. Such fires were rare occurrences and, due to their size, were not expected to be detected by NOAA-20’s VIIRS sensor spatial resolution.

### 2.3 Performance metrics

Verified hotspot detections were used to calculate True Positives (TP) and False Positives (FP), and Missed detections were used to calculate False Negatives (FN). True Negatives (TN) of non-fire pixels were not considered in selection of suitable metrics because the inclusion would make the sample biased towards the relatively easy detection of non-events and inflate the score. Furthermore, the TN would be in any case dependent on the size of Sentinel-2 tiles. The metrics used to evaluate performance of the satellite product

are summarized in Table 2. Precision indicates the portion of reported fires which were verified as correct detections, and Recall indicates which portion of all the real-world fires could be detected by the product. Both these metrics are relevant for policy makers: an algorithm of high precision minimizes mobilization of ground response for false detections, while an algorithm with high recall ensures that fires do not remain undetected. There is often a trade-off between the two, so their harmonic mean (the F1 score) is commonly used to evaluate both of them with a single metric. The Precision-Recall curve graphically describes that trade-off, and the area under this curve (AUC) quantifies the trade-off at different thresholds. More details can be found for example in Luquea et al. (2019) and Saito and Rehmsmeier (2015).

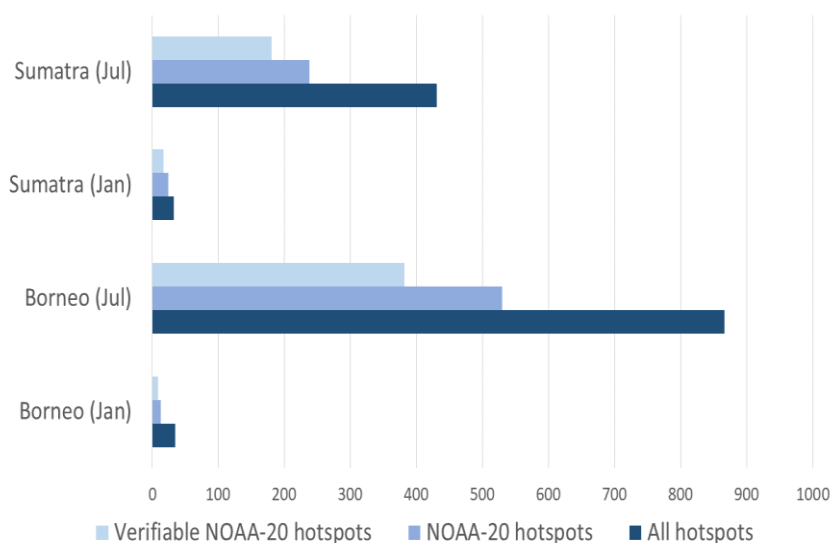


**Figure 3: Number of detected hotspots per island for January and July 2019, including missed detections, correct detections and non-verifiable detections.**

## 2.4 Assessment based on hotspot detection Confidence Levels

The Confidence Levels given by the NOAA-20 active fire product are used to assess the likelihood of false detections. This information can be utilised by recalculating True Positives, False Positives and False Negatives at different confidence thresholds. When a threshold is set to  $T$ , then NOAA-20 detections count as hotspots only if their confidence level exceeds  $T$ . Precision-Recall curves are used at different thresholds to evaluate the trade-off between the two metrics (Saito and Rehmsmeier, 2015) and the relation between the reported Fire Radiative Power (FRP) and detection confidence is examined.

## 3 RESULTS

With visual inspection of a total of 162 Sentinel-2 images over Sumatra and Borneo and for both January and July 2019, 1149 observations were verified, of which NOAA-20 detected 589 (436 TP and 153 FP) and missed 560 (FN). 216 NOAA-20 hotspot detections were classified as non-verifiable due to persistent cloud cover or partial data availability in the tile area. More detections were reported in July (1297, of which 1092 verifiable) than in January (68, of which 57 verifiable), with July being a drier month in Borneo and Sumatra. Overall, the number of verified hotspots in Borneo (749) was almost double the number recorded in Sumatra (400). Detailed numbers of hotspots in each of the examined tile areas are shown in Figure 3.

The distribution of FRP of detected NOAA-20 hotspots differs between Sumatra and Borneo, as well as in different seasons (Figure 4). FRP estimates relate directly to fuel consumption and smoke emission (Xu et al., 2017) and indicate the rate of combustion. Type of fuel, fuel availability, and spatial extent of the fire within a pixel may contribute to FRP. Mean FRP is lower in January than in July, and in July also FRP variability is higher. No clear differences were found between mean FRP in Sumatra and Borneo. These observations may be related to the differences in available fuel or combustion rate between different seasons, local differences in fuel type and the presence of fire in small agricultural parcels as compared to fire in larger, forested areas. Considering the limited sampling area and period, these findings are indicative but not necessarily representative of typical fire patterns on the two islands.

Regarding the relationship between FRP and detection confidence, it was noted that low radiative active fires (FRP < 20 MW) were detected with moderate to high levels of confidence (Figure 5, left panel). In fact, most of the reported hotspots had FRP lower than 20 MW and were detected with a confidence between 60-90%. Increasing FRP coincided with the detection of hotspots with very high confidence level (>90%). On the other hand, most False Positives were found among hotspots with low FRP and detection confidence (Figure 5, right panel). False Positives had a mean FRP of 16 and were reported with a mean Confidence Level of 67%.

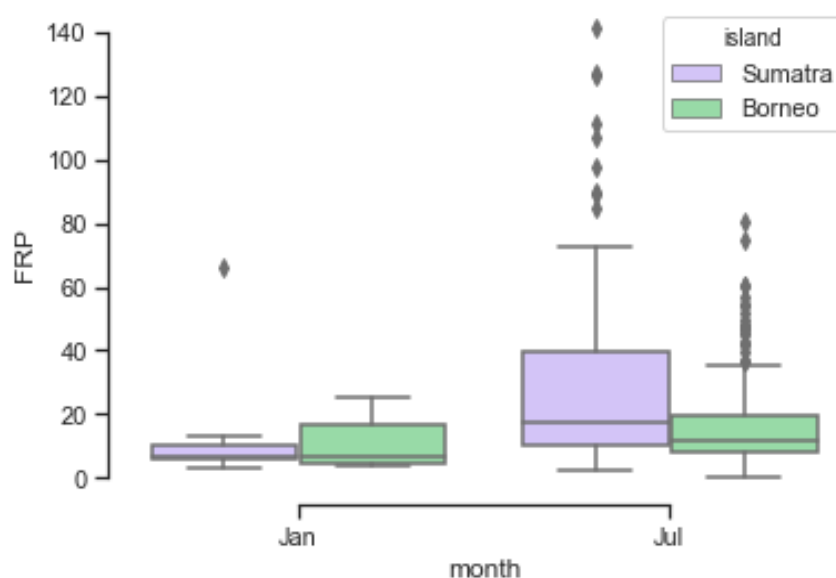


**Figure 4: Boxplot of Fire Radiating Power (FRP) of NOAA-20 detected hotspots over Sumatra and Borneo for January and July 2019. FRP statistics do not include False Positives.**

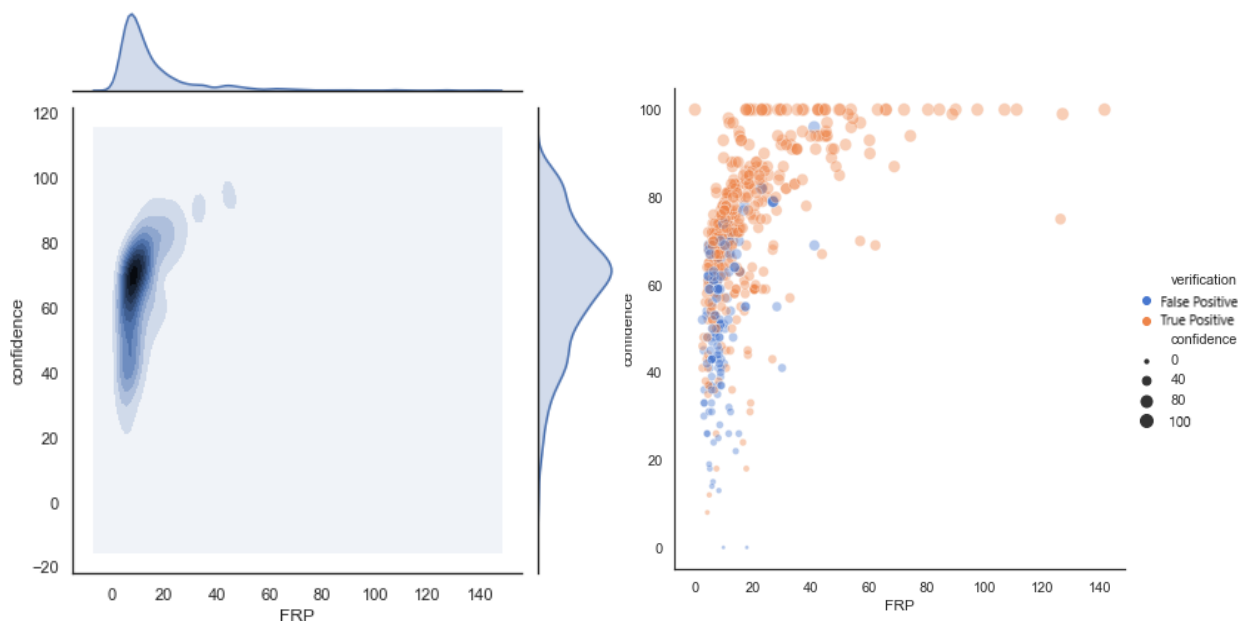


**Figure 5: (Left image) Bivariate distribution of Fire Radiating Power (FRP) and detection confidence for NOAA-20 hotspots, based on kernel density estimation. (Right image) Scatterplot of the same FRP and confidence values, with different colours assigned to True and False Positives after verification.**

Numbers of True and False Positives and False Negatives, Precision values, Recall values and F1 scores, calculated based on the verifiable hotspots for different locations and months, are summarized in Table 3.

The use of stricter confidence thresholds for hotspot detection leads to an increase in Precision (Figure 6). Higher precision indicates a decrease of False Positives, while decreasing Recall could mean that more fires remain undetected.

#### 4 DISCUSSION AND CONCLUSIONS

This study is a preliminary assessment of the new operational *NOAA-20/JPSS-1 Active Fires* product, specifically for areas in Southeast Asia close to Singapore, which are characterized by regular high fire occurrence that may potentially affect air quality in Singapore. It should be noted that verification is done only with Sentinel-2 data, due to lack of ground truth data. Therefore, the results of our study are not conclusive but rather indicative of product performance.

	January & July		Both locations		
	Sumatra	Borneo	January	July	
TP	130	306	17	419	436
FP	68	85	9	144	153
FN	202	358	31	529	560
<b>Total</b>	<b>400</b>	<b>749</b>	<b>57</b>	<b>1092</b>	<b>1149</b>
Precision	0.66	0.78	0.65	0.74	0.74
Recall	0.39	0.46	0.35	0.44	0.44
F1-score	0.49	0.58	0.46	0.55	0.55
AUC	0.83	0.87	0.78	0.87	0.86

**Table 3: Verification results and relevant metrics for different locations and detection algorithms. The metrics are calculated for fire hotspots at all Confidence Levels**

Considering the hotspots detected by NOAA-20, reported FRP levels are low in comparison to the findings of Xu et al. (2017). This is consistent with the presence of low-radiating agricultural residue burning and/or smouldering peat fires in the area, as described respectively by Xu et al. (2017) and Elvidge et al. (2015). However, low FRP did not seem to hinder detection, as medium- to high confidence levels were recorded even for fires with low FRP. This is important, as hotspots need to be detected as early as possible to minimize damage and to ensure efficient allocation of firefighting resources.

We found differences in terms of the number of hotspots, FRP and detection performance metrics between Sumatra and Borneo and between July and January. These differences may have been partially due to the different number of observations between subsets, but nevertheless seem to support the need to tune the thresholds of detection algorithms locally and seasonally as suggested by Csiszar et al. (2018). Considering the trade-off between correct and missed detections, better product performance was found in July 2019 (dry season) as fires were likely to be more intense and easier to detect.

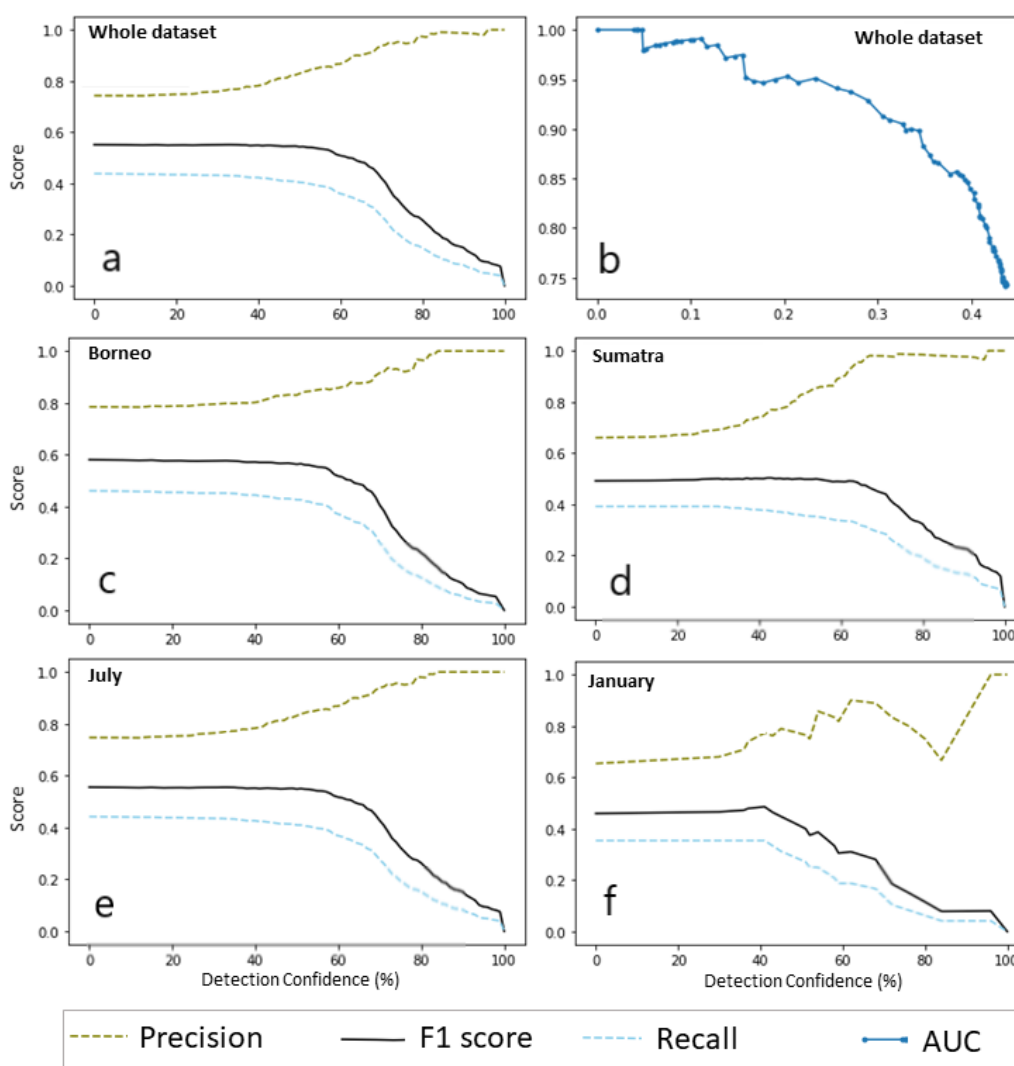


**Figure 6: Performance metrics for the hotspot detection results. In Panel (a), Precision, Recall and F-scores for the whole dataset are calculated at different detection thresholds based on the confidence of reported hotspots. Panel (b) shows the Precision-Recall Curve for the same thresholds, and the Area under the Curve (AUC). Panels (c)-(f) are the same as (a) but have been separated into results for the different islands and months of the analysis. Calculations take into consideration NOAA-20 reported hotspots as well as missed detections (no assigned Confidence Level) registered by visual inspection of Sentinel-2 imagery.**

The Confidence Levels of the algorithm are a heuristic measure determined by the number of adjacent cloud pixels, adjacent water pixels, and temperature thresholds. The verification procedure showed that there are cases of hotspots with very high and very low Confidence Levels which occur almost at the same time and location within actual fires (example D in Figure 2). A possible reason for such occurrences may be that pixels within an active fire area may be obscured by smoke emitted from nearby pixels. Another potential reason may be the presence of clouds in nearby pixels, which would reduce confidence in the detection. To that end, post-processing of registered alarms may help to distinguish low-confidence detections which are located close to high-confidence actual hotspots from others which correspond to False Positives.

The number of undetected fires (FN) in this study is almost as high as the number of registered hotspots (TP and FP), despite the fact that we did not consider fires with extent smaller than 100x100m<sup>2</sup>. The highest F1 scores are obtained when no threshold is imposed on Confidence Levels, but this could mean trading higher Recall (lesser missed detections) values for lower Precision values (more False Positives). This could be desirable to minimize missed detections, and for the user to ensure response to the highest number of fire incidents. In this case, all hotspots reported by the product should be considered regardless of detection Confidence Levels. However, if the *Active Fires* product is used to reduce mobilization of ground response teams for false positives, detection confidence information may be useful. Using a 70% confidence cut-off, for example, 96% of declared hotspots correspond to confirmed fires. Users could make use of such information to make decisions based on their risk appetite for different scenarios and the associated cost-benefit analyses.

The most common potential source of missed detections is the presence of smoke or clouds. On the other hand, most of the recorded false positives included cloud edges and bright surfaces in the vicinity of water pixels. Tuning background characterization for the algorithm with respect to these sources of error could improve detection results, as suggested by Tsidulko et al. (2019), and this could lead to improved performance tailored to our region. It would thus be useful to include in future research more regions in Southeast Asia, comparison between night-time and day-time algorithm assessments, and ground-truth data wherever available. Finally, a database of verified hotspot detections can

serve as a label dataset to train supervised algorithms for automated hotspot detection in the future.

## 5 REFERENCES

- Amos, C., Petropoulos, G. and Ferentinos, K. (2019) 'Determining the use of Sentinel-2A MSI for wildfire burning and severity detection', *International Journal of Remote Sensing*, 40(3), pp. 905-930.
- Atzberger, C. (2016) 'First experiences with European Sentinel-2 multi-spectral imager (MSI)', *Remote Sensing*, Issue Special Issue (ISSN 2072-4292).
- Cicala, L., Angelino, C., Fiscante, N. and Ullo, S. (2018) 'Landsat-8 and Sentinel-2 for fire monitoring at local scale: a case study on Vesuvius', *IEEE International Conference on Environmental Engineering*.
- Csiszar, I., Morisette, J. and Giglio, L. (2006) 'Validation of active fire detection from moderate-resolution satellite sensors: The MODIS example in Northern Eurasia', *IEEE Transactions on Geoscience and Remote Sensing*, 44(7), pp. 1757- 1764.
- Csiszar, I., Schroeder, W., Giglio, L., Ellicott, E., Vadrevu, K., Justice, C. and Wind, B. (2013) 'Active fires from the Suomi NPP Visible Infrared Imaging Radiometer Suite: Product status and first evaluation results', *Journal of Geophysical Research (Atmospheres)*, Volume 119, pp. 803-816.
- Csiszar, I., Tsidulko, M. and Schroeder, W. e. a., (2018), 'Beta maturity status declaration for NOAA-20 VIIRS Active Fire EDR', s.l.: NOAA. (retrieved from [https://www.star.nesdis.noaa.gov/jpss/documents/AMM/N20/Land\\_ActiveFires\\_Beta\\_Provisional\\_ReadMe.pdf](https://www.star.nesdis.noaa.gov/jpss/documents/AMM/N20/Land_ActiveFires_Beta_Provisional_ReadMe.pdf))
- Elvidge, C., Zhizhin, M., Hsu, F.-C., Baugh, K., Khomarudin, R., Vetruta, Y., Sofan, P., Suwarsono, S. and Hilman, D. (2015) 'Longwave Infra-red identification of smoldering peat fires in Indonesia with nighttime LANDSAT data', *Environmental Research Letters*, 10(6).
- Filipponi, F. (2019) 'Exploitation of Sentinel-2 Time Series to Map Burned Areas at the National Level: A Case Study on the 2017 Italy Wildfires. *Remote Sensing*', 11(6), p. 622.
- Liu, Y., Stanturf, J. and Goodrick, S. (2010) 'Trends in global wildfire potential in a changing climate', *Forest Ecology and Management*, Volume 259, pp. 685-697.

- Luquea, A., Carrasco, A., Martina, A. and de la Heras, A. (2019) 'The impact of class imbalance in classification performance metrics based on the binary confusion matrix', *Pattern Recognition*, Volume 91, pp. 216-231.
- Reid, J., Hyer, E., Johnson, R., Holben, B., Yokelson, R., Zhang, J., Campbell, J., Christopher, S., Di Girolamo, L., Giglio, L., Holz, R., Kearney, C., Miettinen, J., Reid, E., Turk, J., Wang, J., Xian, P., Zhao, G., Balasubramanian, R., Chew, B., Janjai, S., Lagrosas, N., Lestari, P., Lin, N., Mahmud, M., Nguyen, A., Norris, B., Nguyen, O., Min Oo, Salinas, S., Welton, E. and Liew, S. (2013) 'Observing and understanding the Southeast Asian aerosol system by remote sensing: An initial review and analysis for the Seven Southeast Asian Studies (7SEAS) program', *Atmospheric Research*, Volume 122, pp. 403-468.
- Roteta, E., Bastarrika, A., Padilla, M., Storm, T. and Chuvieco, E. (2019) 'Development of a Sentinel-2 burned area algorithm: Generation of a small fire database for sub-Saharan Africa', *Remote Sensing of the Environment*, Volume 222, pp. 1-17.
- Saito, T. and Rehmsmeier, M. (2015) 'The Precision-Recall curve is more informative than the ROC Plot when evaluating binary classifiers on imbalanced datasets', *PLoS ONE*, 10(3).
- Schauman, S., Verger, A., Filella, I. and Peñuelas, J. (2018) 'Characterisation of functional trait dynamics at high spatial resolution in mediterranean forest from Sentinel-2 and ground-truth data', *Remote Sensing*, 10(12), p. 1874.
- Schmetz, J. and Menzel, P. (2015) 'A look at the evolution of Meteorological Satellites: Advancing capabilities and meeting user requirements', *Weather, Climate and Society*, Volume 7, pp. 309-320.
- Schroeder, W., Oliva, P., Giglio, L. and Csiszar, I. (2014) 'The New VIIRS 375m active fire detection data product: Algorithm description and initial assessment', *Remote Sensing of Environment*, Volume 143, pp. 85-96.
- Tsidulko, M., Csiszar, I. and Schroeder, W. (2019) 'VIIRS Active Fire Products in NOAA JPPS Suite: Potential Algorithm Improvement in Specific Fire Scenarios', San Francisco, AGU Fall Meeting Abstracts.
- Xu, W., Wooster, M., Kaneko, T., He, J., Zhang, T. and Fisher, D. (2017) 'Major advances in geostationary fire radiative power (FRP) retrieval over Asia and Australia stemming from the use of Himawari-8 AHI', *Remote Sensing of the Environment*, Volume 193, pp. 138-149.
- Yuhendra and Yulianti, E. (2019) 'Multi-temporal Sentinel-2 images for classification accuracy', *Journal of Computer Science*, 15(2), pp. 258-268.

# Understanding the impact of transboundary haze on surface solar irradiance in Singapore

Chia Zhong Yi, Christopher Gan

Centre for Climate Research Singapore, Meteorological Service Singapore

## ABSTRACT

During transboundary haze episodes, local visibility in Singapore is often reduced due to visible light scattering by airborne haze particles. This scattering also affects the transmissivity of the atmosphere, which implies that solar irradiance received by solar panels is affected by the presence of airborne haze particles. To investigate the impact of haze on the transmissivity of the atmosphere, the statistical distributions of clearness index (the transmissivity of the atmosphere) during hazy and non-hazy days were compared. A two-sample Kolmogorov-Smirnov (K-S) test demonstrated that haze particles do affect the transmissivity of the atmosphere. However, the analysis showed that even during hazy periods, cloud cover remains an important factor in solar forecasting. The findings suggest that an effective solar forecasting system for hazy periods must be able to predict both haze particle concentrations and cloud spatial distributions reliably.

## 1 INTRODUCTION

Singapore has experienced recurrent transboundary haze episodes in the past few decades due to land and vegetation fires in the region. Some of the most severe haze episodes have coincided with strong El Niño events (Forsyth, 2004). During haze episodes, the concentration of aerosol particles in the atmosphere can increase by multiple folds relative to normal conditions (Figure 1), as was evident during the severe haze episodes in 2013 and 2015. High aerosol concentrations<sup>1</sup> reduce visibility due to aerosol scattering effects in the visible band (Lee et al., 2016). This implies that high aerosol concentrations would similarly affect the transmissivity of the atmosphere and the energy generated by solar panels.

<sup>1</sup> Lee et al., 2016 reported that although aerosol concentrations are the primary attenuating factor, relative humidity exerts an influence on visibility due to hygroscopic growth of aerosol particles. The focus of this study, however, is on the clearness index instead of visibility, and the attenuation of mostly downward propagating shortwave radiation rather than

To understand this impact, the difference in clearness index between hazy and non-hazy periods needs to be analysed.

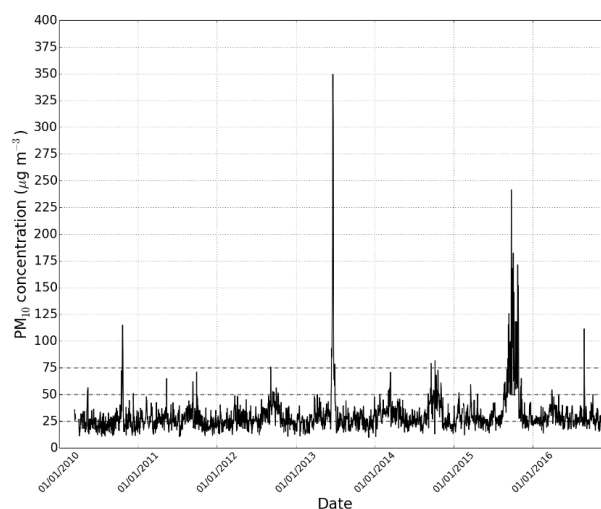


**Figure 1: 12-hour Island wide averaged PM<sub>10</sub> concentration from 2010 to 2016. PM<sub>10</sub> concentrations of 25, 50 and 75  $\mu\text{g m}^{-3}$  are marked with horizontal dashed lines.**

While higher aerosol concentrations would lead to an increase in visible light scattering, this would not necessarily mean a reduction in the clearness index. Global Horizontal Irradiance (GHI), a measure of the irradiance received by solar panels, can be broken down into two components – Direct Normal Irradiance (DNI; the forward propagating component) and Diffuse Horizontal Irradiance (DHI; the diffuse component). Stronger scattering reduces the DNI component, but at the same time could enhance the DHI component. This implies that the relationship between higher aerosol concentrations in the atmosphere and GHI can be complicated.

horizontally propagating visible light. As the primary attenuation factor on clearness index is cloud cover, aerosol concentration and relative humidity become secondary and tertiary factors respectively. Therefore, the effect of relative humidity has been excluded in this study.

Apart from aerosols, clouds play a significant role in attenuating the incoming solar irradiance mainly through shortwave scattering processes (Matuszko, 2012). The scattering processes change the direction of the downward-propagating shortwave radiation from the sun and hence reduce the total amount of solar irradiance reaching the surface. A separate study on the cloud attenuation effect in Singapore was previously conducted and documented (Chia, 2019), and the results suggest that cloud spatial distribution greatly influences the uncertainty in irradiance forecasts. This is especially notable in the equatorial region given there is ubiquitous cloud cover during normal climatological conditions and often rapid convective cloud formation. The amount of cloud cover during hazy periods could differ from normal climatological conditions. A severe haze episode often coincides with a strong El Niño event, during which the region tends to be less cloudy than usual (Harrison and Chiodi, 2015). During hazy periods, both the variability in cloud cover and aerosol concentrations will collectively influence the clearness index. The relative impact of these two factors during hazy periods is examined in this study.

## 2 DATA AND METHODS

### 2.1 Data

PM<sub>10</sub> concentrations measured at ambient air quality monitoring sites, and observations of GHI and cloud cover from meteorological stations in Singapore for the

years 2010 to 2016 were analysed in this study. The station locations are shown in Figure 2.

As the air quality and meteorological stations are not collocated, PM<sub>10</sub> concentrations and GHI are measured at separate locations. During haze episodes, there could be hour-to-hour fluctuations in PM<sub>10</sub> concentrations across stations. For a particular hour, it means the PM<sub>10</sub> concentration measured by an air quality station may not be representative of the concentration over the nearest meteorological station measuring GHI.

The impact of such differences can be mitigated by averaging the data in both space and time. In this study, the 12-hour island wide average of each variable observed during the daytime is used (as GHI goes to zero at night). The 12-hour average is taken from 7 am to 7 pm – centred at 1 pm, which is the true solar noon time in Singapore.

#### 2.1.1 Clearness index

Clearness index is a measure of the atmospheric transmissivity of solar irradiance. It is defined as the observed GHI at a station divided by the incoming solar irradiance assuming the atmosphere is absent. This irradiance is calculated based on the orbital dynamics of the Earth (Iqbal, 1983), assuming a solar constant of  $1365 \text{ W m}^{-2}$ . When attenuating factors such as clouds are present in the atmosphere, the clearness index will be lower and the GHI will consequently be weaker.

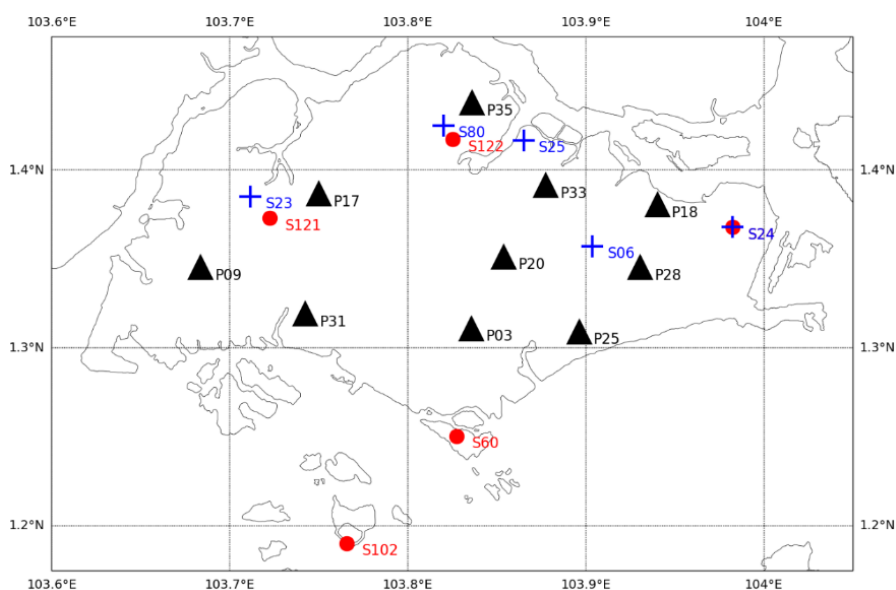


**Figure 2: Locations of selected stations that record global horizontal irradiance (red circles), cloud cover (blue crosses) and PM<sub>10</sub> concentrations (black triangles). Note that S24 records both global horizontal irradiance and cloud cover.**

### 2.1.2 Cloud cover

Clouds have a major influence on clearness index (Matuszko, 2012 and Chia, 2019). Cloud observations used in this report are recorded hourly by human observers based on guidelines specified in the International Cloud Atlas published by the World Meteorological Organization (WMO). The amount of cloud cover is reported in the unit of oktas with values ranging from 0 to 8 (WMO, 1975, 1987). Clouds are categorised into low, middle or high level clouds as defined by having a base height of below 2 km, between 2 and 6 km and above 6 km, respectively. High level clouds have been excluded in this study because they are generally ice clouds and have much less impact on visible light compared to lower level clouds (Matuszko, 2012).

### 2.1.3 PM<sub>10</sub> concentration

PM<sub>10</sub> concentrations were used as the indicator of hazy conditions. PM<sub>10</sub> concentration is defined as the total mass per unit air of aerosol particles with diameters of 10 µm or smaller (Hinds, 1998). As PM<sub>10</sub> comprises a larger range of particle sizes compared to PM<sub>2.5</sub>, it is a more comprehensive choice for the analysis of scattering effects. The mass contributed by PM<sub>2.5</sub> (particles with diameters of 2.5 µm or smaller) is a subset of PM<sub>10</sub> concentrations.

While only PM<sub>10</sub> measurements at ground level were considered in this study, aerosol concentrations at higher levels could also contribute to the scattering effect (Chew et al., 2013). However, significant correlation has been found between aerosol optical depths (a measure of aerosol scattering effect) within the entire atmospheric column and surface aerosol concentration, even at an hourly timescale (Chew et al., 2011). This suggests that surface aerosol concentrations at the daily timescale analysed in this study can account for the variation of aerosol scattering effects within the atmospheric column.

## 2.2 Probability distribution of clearness index

Probability distributions of clearness index using 12-hour island wide averaged clearness index data were studied under different atmospheric conditions. The atmospheric conditions were first differentiated as “normal periods” and “hazy periods”. These were further sub-divided into the following: “normal periods

with few clouds”, “normal periods with more clouds”, “hazy periods with few clouds” and “hazy periods with more clouds”. The cloud conditions were defined based on cloud cover amounts being higher or lower than specific thresholds. Details on the cloud thresholds are discussed in Sec. 3.4.1.

### 2.2.1 Discrete probability and cumulative distribution functions

To construct the probability distributions, histograms of clearness index with bin size of 0.05 were used so that discrete cumulative distribution functions can be estimated. The discrete probability functions were subsequently deduced from the discrete cumulative distribution functions using first-order central finite differences.

### 2.2.2 Quantile-quantile plot comparison

To analyse pairs of probability distributions under the different atmospheric conditions, quantile-quantile (Q-Q) plots were used. In a Q-Q plot, the quantiles<sup>2</sup> of one distribution are compared against the quantiles of another distribution. If the data points sit on the identity line<sup>3</sup>, then the two distributions are identical.

## 2.3 Probability distribution of cloud cover

The discrete probability functions of cloud cover under different atmospheric conditions were constructed by building 2D-histograms of cloud cover with bin size of 0.5 okta. 12-hour Island wide averaged low and middle cloud cover data that met the specified atmospheric condition were analysed.

## 2.4 Two-sample Kolmogorov-Smirnov test

The two-sample Kolmogorov-Smirnov (K-S) test is a one-sided statistical test for determining if a difference exists in two empirical probability distributions constructed from different data sets (Wilks, 2011). The null hypothesis to be rejected is that the two empirical distributions are the same but come from an unspecified distribution.

In this test, the largest absolute difference between the empirical cumulative distribution functions ( $D_s$ ) is identified.

<sup>2</sup> For example, the 25%-quantile of a clearness index distribution is the value in which 25% of samples have clearness index smaller or equal to the value.

<sup>3</sup> A straight line passing through the origin with a gradient of one.

$$D_s > \sqrt{-\frac{1}{2} \left( \frac{1}{n_1} + \frac{1}{n_2} \right) \ln \left| \frac{\alpha}{2} \right|}$$

where  $\alpha$  is the rejection level with a range from 0 to 1,  $n_1$  and  $n_2$  are the numbers of sample points in the two distributions. In this statistical test, the null hypothesis can be rejected with  $\alpha \times 100\%$  rejection level<sup>4</sup>.

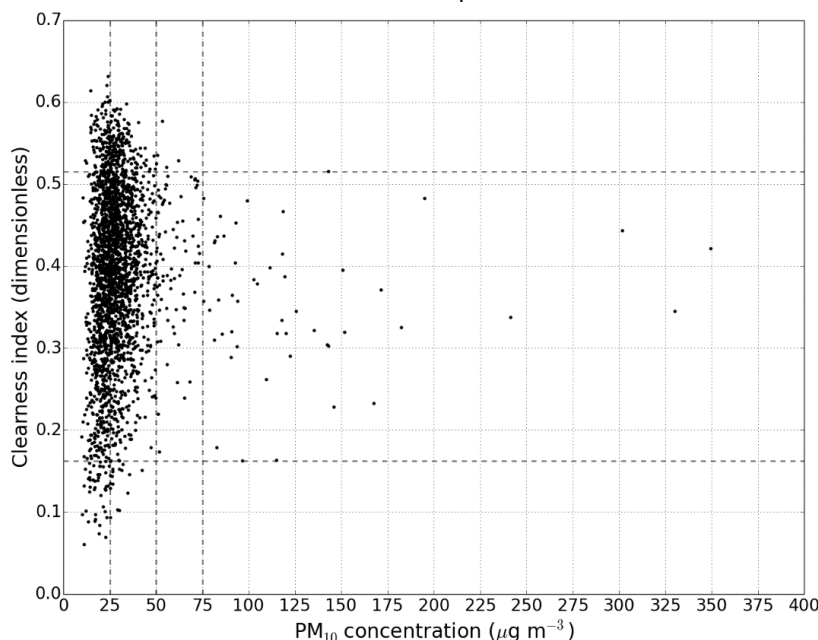


**Figure 3: Scatter plot of PM10 concentrations versus clearness index. Both quantities are 12-hour island wide averages during daytime (7 am to 7 pm). PM10 concentrations of 25, 50 and 75  $\mu\text{g m}^{-3}$  are marked with vertical dashed lines. The maximum and minimum clearness index with PM10 values larger than 75  $\mu\text{g m}^{-3}$  are marked with horizontal dashed lines.**

### 3 RESULTS AND DISCUSSION

#### 3.1 Relationship between PM10 and clearness index

The daytime relation between island wide averaged clearness index and PM<sub>10</sub> concentrations is shown in Figure 3. The majority of sample points are at PM<sub>10</sub> concentrations < 50  $\mu\text{g m}^{-3}$ . At PM<sub>10</sub> concentrations  $\geq$  50  $\mu\text{g m}^{-3}$ , data points become increasingly sparse. This is similarly reflected in Figure 1, where PM<sub>10</sub> concentrations are generally below 50  $\mu\text{g m}^{-3}$ .

At PM<sub>10</sub> concentrations < 25  $\mu\text{g m}^{-3}$ , the range of clearness index values is the most widespread, ranging from approximately 0.05 to 0.65. From PM<sub>10</sub> concentrations of 25  $\mu\text{g m}^{-3}$  to 50  $\mu\text{g m}^{-3}$ , there is a reduction in the range of clearness index (the maximum of clearness index decreases and the minimum

increases). However, this trend is less apparent in the region where PM<sub>10</sub> concentrations are between 50 and 75  $\mu\text{g m}^{-3}$ . Beyond PM<sub>10</sub> concentrations of 75  $\mu\text{g m}^{-3}$ , there are insufficient data points to deduce if this narrowing trend extends to higher concentrations. The findings indicate that the probability of extreme GHI values (very bright or very dim days) is lower during hazy periods.

#### 3.2 Differentiating normal and hazy periods

Based on the above discussion, PM<sub>10</sub> concentrations of 50 and 75  $\mu\text{g m}^{-3}$  are potential thresholds to indicate transitions in the clearness index distribution with respect to increasing concentrations. However, the 75  $\mu\text{g m}^{-3}$  threshold is likely to be too stringent as it excludes several less severe haze days (i.e. peaks between 50 and 75  $\mu\text{g m}^{-3}$  in Figure 1). Therefore, a PM<sub>10</sub> concentration threshold of 50  $\mu\text{g m}^{-3}$  was selected to define a hazy period in this study. This threshold is similar to the World Health Organization (WHO) recommended target (WHO, 2017), but is a 12-hour daytime average instead of the 24-hour average used by WHO. Based on this threshold, there are 2321 and 134 sample points respectively in normal and hazy periods over the seven-year period.

<sup>4</sup> A lower value in the rejection level indicates a more stringent statistical test.

### 3.3 Comparison of normal and hazy periods

To investigate the difference in clearness index between normal and hazy periods, probability distributions of clearness index were constructed for the respective periods. The discrete probability functions, together with the probability function constructed using sample points for all periods are shown in Figure 4.

cloud cover between the two periods clearly shows that there are fewer low level clouds during hazy periods. The most probable amount of low cloud cover changes from approximately 3.25 oktas during normal periods to 1.5 oktas during hazy periods, but remains similar for middle cloud cover. With fewer low level clouds during hazy periods, the cloud obscuration effect is weakened. This partially explains the lower occurrence of dim events during hazy periods, but not the lower occurrence of

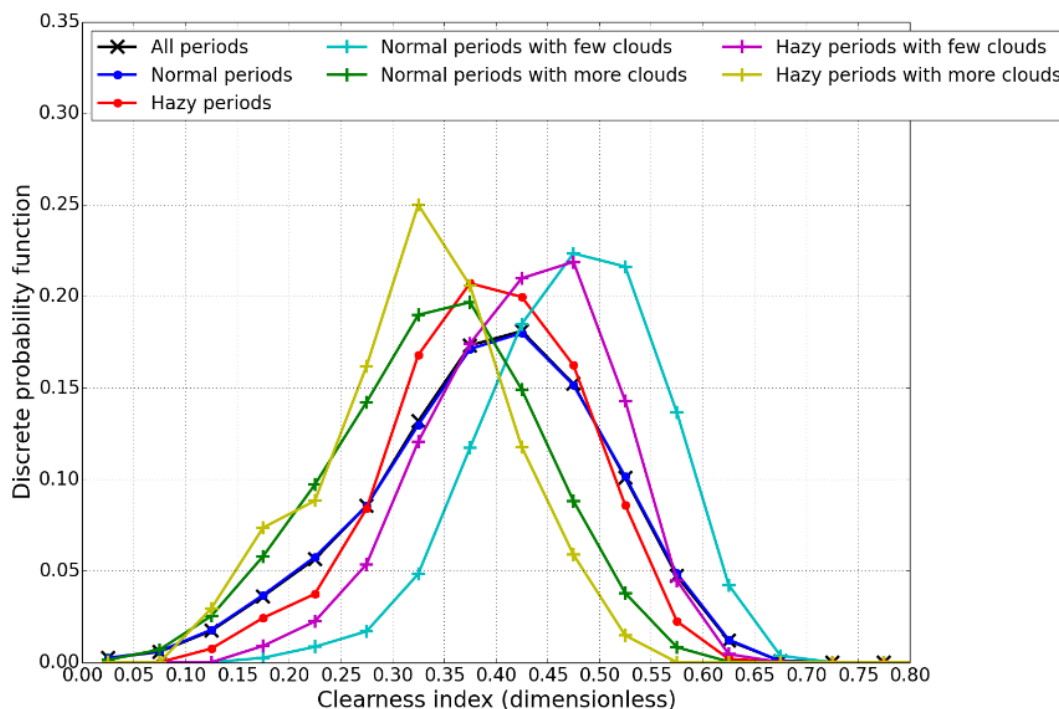


Figure 4: Discrete probability functions of daytime clearness index under different atmospheric conditions.

In Figure 4, the distributions during “all periods” (black) and “normal periods” (blue) are largely similar as most of the days fall under normal periods. The clearness index distribution of hazy periods (red) appears to be less widespread compared to normal periods. This supports the earlier notion in Sec. 3.1 that the variability of clearness index is constrained during hazy periods. However, the effect of clouds should be considered, as cloud cover patterns during hazy periods may be different and hence affect the variability of the clearness index as well.

### 3.4 Impact of differences in cloud amount

To understand the impact of differences in cloud amount, the probability distributions of daytime 12-hour averaged cloud cover during normal (Figure 5a) and hazy periods (Figure 5b) were compared. Due to the limited number of sample points available during hazy periods, the probability distribution is less distinct as compared to normal periods. Nevertheless, the comparison of

bright events.

#### 3.4.1 Excluding impact from cloud amount differences

In order to isolate the impact of haze on clearness index, the impact of differences in cloud amount should be excluded as much as possible. This can be achieved by comparing the clearness index distributions when there were very few clouds in the sky. Sample points with cloud cover less than a certain threshold were then chosen to construct clearness index distributions for both normal and hazy periods.

The thresholds of cloud cover were derived based on the probabilities shown in Figure 5a and Figure 5b. For middle cloud cover, the distribution appears similar for both normal and hazy periods and a threshold of 1 okta was chosen for simplicity. For low cloud cover, in cases when middle cloud cover is less than 1 okta, there is an increasing probability of low cloud cover from 0 to 3.5

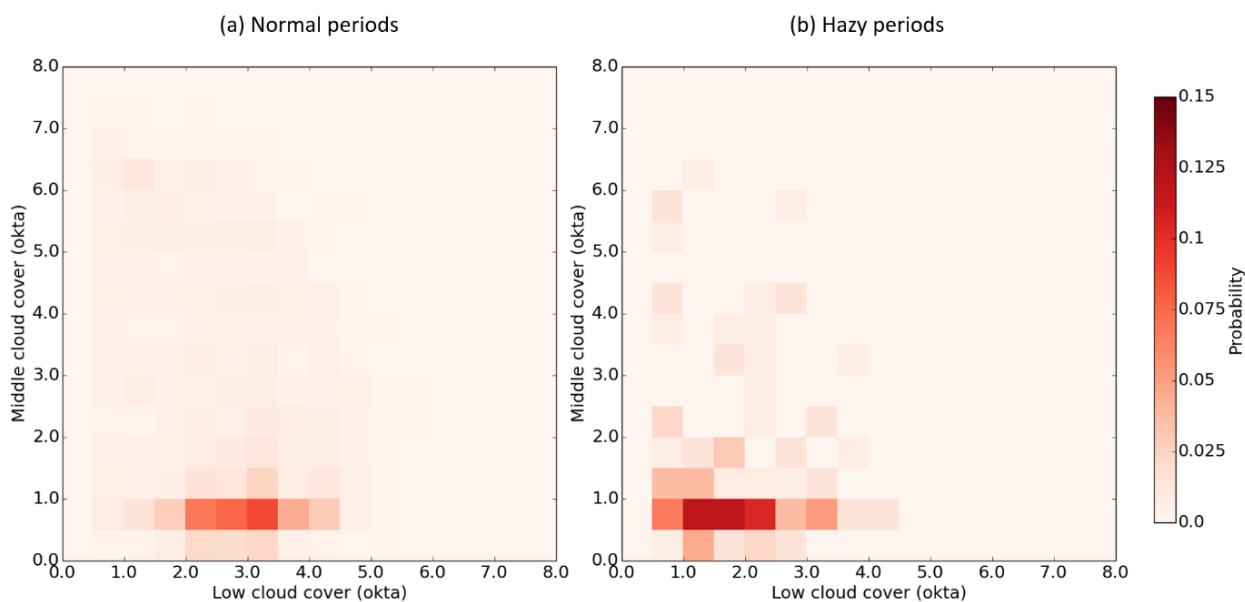


**Figure 5: The probability of 12-hour averaged low and middle cloud cover.**

oktas during normal periods (Figure 5a). During hazy periods (Figure 5b), the same probability shows an increasing trend only up to around 2 oktas. To achieve a threshold such that the cloud distributions created from the remaining sample points were similar for both normal and hazy periods, a low cloud cover threshold of 2 oktas was selected. This is illustrated in the resulting cloud probability distributions for normal and hazy periods shown in Figure 6a and Figure 6b, constructed with 146 and 50 samples respectively. On the other hand, the selected thresholds are also effective in separating the cases with few and more clouds during normal periods. As shown in Figure 4, the former’s clearness index distribution (cyan line) clearly sits at the brighter end compared to the latter’s (green line). The result agrees with our expectation that clouds attenuate surface solar irradiance (at 12-hour timescale).

### 3.5 Impact from haze only

With only the sample points taken under few clouds retained, the clearness index distribution of normal periods (magenta) and hazy periods (cyan) can be compared in Figure 4. The two distributions appear to share a similar shape but the distribution for hazy periods is shifted towards lower clearness index values. Examining the two distributions further in a Q-Q plot (Figure 7), the points are nearly parallel to the identity line but displaced slightly towards the axis of normal periods. This suggests that haze has an overall attenuating effect on the clearness index. Assuming the same cloud distribution, it can therefore be concluded that a hazy period will likely be dimmer than a normal period.

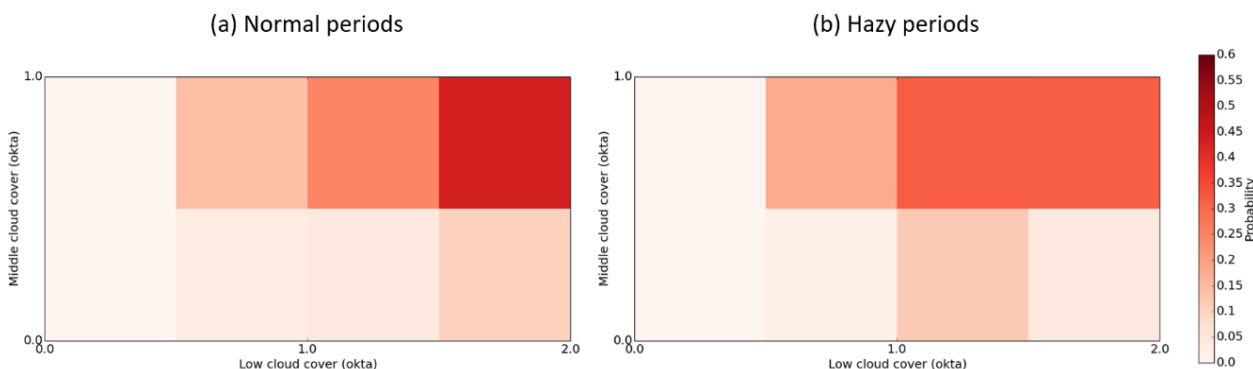


**Figure 6: The probability of 12-hour averaged low and middle cloud cover, when there are relatively few clouds.**

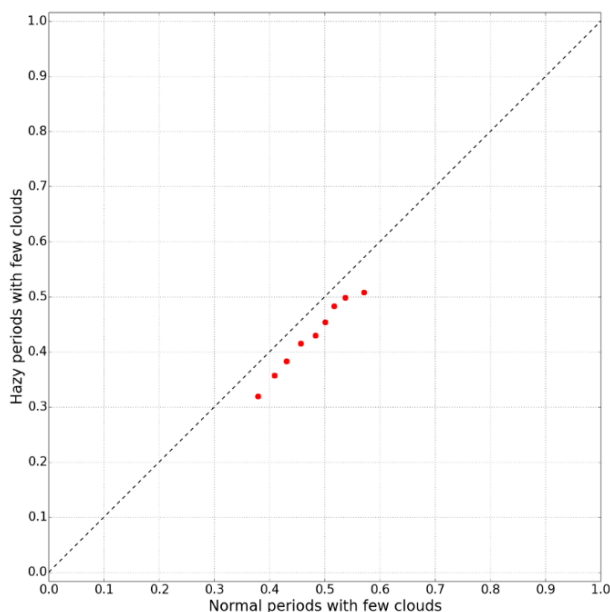


**Figure 7: Quantile-quantile plot of clearness index distributions of normal and hazy periods with few clouds. The data points from the 10<sup>th</sup> to 90<sup>th</sup> percentiles (inclusive) with equal spacing are plotted.**

To verify that haze does have an impact on the clearness index, a two-sample K-S test is performed as described in Sec. 2.4. The null hypothesis to be rejected is that the clearness index distributions of normal and hazy periods with few clouds are the same. With  $D_s = 0.22$  at 47.5-percentile (see Figure 8),  $n_1 = 146$  and  $n_2 = 50$ , the null hypothesis can be rejected at a rejection level of 10% (the p-value is 0.06 given the null hypothesis). This test could be improved in future if the datasets are accumulated over a longer period of time.

atmosphere, it is designed to better capture the variation in DNI (the forward propagating component of GHI) rather than DHI (the diffuse component). Due to increased aerosol concentrations and their scattering effect during hazy periods, DHI could be a more important factor but its variability is not well represented by the clearness index. Nevertheless, a similar conclusion that air pollution can attenuate surface solar irradiance has also been found in a study conducted in eastern China (Li et al., 2017).

A point on the use of clearness index in this study needs to be highlighted. Since clearness index is the ratio between GHI and incident irradiance at the top of the

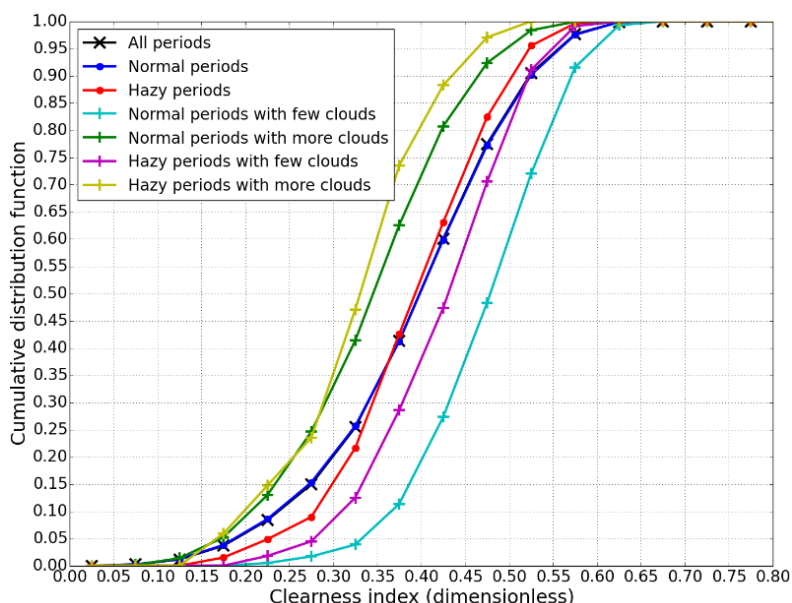


**Figure 8: Cumulative distribution functions of daytime clearness index under different atmospheric conditions.**

### 3.6 Impact of clouds during hazy periods

For a more complete analysis of hazy periods, the clearness index distribution during hazy periods with more clouds is also shown in Figure 4 (yellow). This distribution is shifted towards the far dimmer side compared to both hazy and normal periods with few

during hazy periods is shifted towards dimmer conditions. This suggests that haze has an overall attenuating effect on the clearness index and hence GHI. However, cloud attenuation effects remain important even during hazy periods and an effective solar forecasting system must be able to predict both the haze and cloud spatial distributions reliably.

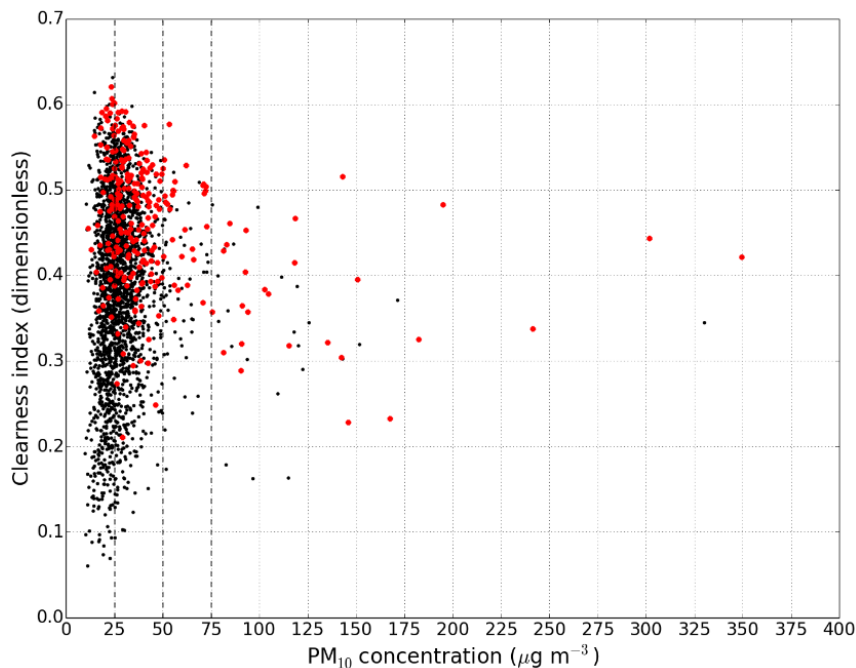


**Figure 9: Scatter plot of PM10 concentration versus clearness index during daytime. Larger red dots represent sample points taken under few cloud conditions.**

clouds. While this suggests that cloud attenuation effects could be stronger compared to haze, it is difficult to draw such a conclusion based on this analysis alone. Under such atmospheric conditions, the  $PM_{10}$  concentrations can range from fifty to hundreds of  $\mu g m^{-3}$  (Figure 9), middle cloud cover can range from around 1 to 6 oktas and low cloud cover can range from around 2 to 5 oktas (Figure 5b). Furthermore, the limited number of sample points available is insufficient to discern the respective attenuation effects of haze and cloud.

## 4 SUMMARY

In this study, daytime hours from 2010 to 2016 were categorised into normal or hazy periods. A  $PM_{10}$  concentration threshold of  $50 \mu g m^{-3}$  was selected to define hazy conditions. During hazy periods, the discrete probability distribution was shown to be sharper compared to normal periods. The reduced probability of dim events may partially be explained by the presence of fewer clouds during hazy periods. When examining only cases when there are few clouds in the sky, both distributions share a similar shape but the distribution

## 5 REFERENCES

- Chew, B., Campbell, J., Hyer, E., Salinas, S., Reid, J., Welton, E., Holben, B. and Liew, S.C. (2016) 'Relationship between Aerosol Optical Depth and Particulate Matter over Singapore: Effects of Aerosol Vertical Distributions', *Aerosol and Air Quality Research*, vol. 16, pp. 2818-2830.
- Chia, Z.-Y (2019) 'Cloud obscuration effective irradiance report', A deliverable of NUS/NEA collaboration on Solar Power Forecasting for Energy Market Authority, Singapore.
- Chiodi, A.M. and Harrison, D. (2015) 'Global seasonal precipitation anomalies robustly associated with El Nino and La Nina Events - An OLR perspective', *Journal of Climate*, vol. 28, pp. 6133-6159.
- Forsyth, T. (2014) 'Public concerns about transboundary haze: A comparison of Indonesia,

Singapore and Malaysia', *Global Environmental Change*, vol. 25, pp. 76-86.

Iqbal, M. (1983) *An introduction to solar radiation*, Academic Press.

Lee, S.-Y, Gan, C. and Chew, B.N. (2016) 'Visibility deterioration and hygroscopic growth of biomass burning aerosols over a tropical coastal city: a case study over Singapore's airport', *Atmos. Sci. Let.*, vol. 17, pp. 624-629.

Li, X., Wagner, F., Peng, W., Yang, J. and Mauzerall, D. (2017) 'Reduction of solar photovoltaic resources due to air pollution in China', *PNAS*, vol. 114, no. 45, pp. 11867-11872.

Matuszko, D. (2012) 'Influence of the extent and genera of cloud cover on solar radiation intensity', *Int. J. Climatol.*, vol. 32, pp. 2403-2414.

Wilks, D.S. (2011) *Statistical methods in the atmospheric sciences*, Academic Press.

World Health Organization Regional Office for Europe (2017) 'Evolution of WHO air quality guidelines: Past, present and future'.

World Meteorological Organization, *International Cloud Atlas Volume I*, Geneva, 1975.

World Meteorological Organization, *International Cloud Atlas Volume II*, Geneva, 1987.

# An anthropogenic heat flux emission inventory for Singapore for urban climate modelling

Andrés Simón-Moral, Matthias Roth

Department of Geography, National University of Singapore, Singapore

## ABSTRACT

An inventory-based anthropogenic heat flux ( $Q_F$ ) database is estimated for Singapore for 2016. A combination of top-down and bottom-up approaches is used to estimate the hourly  $Q_F$  from residential and non-residential buildings, light and heavy industry, road traffic and railway network. A diurnal profile is further calculated and applied to the entire urban area to obtain the diurnal cycle of  $Q_F$ . The results are calculated for a 300 m resolution grid and are ready to be implemented in the MORUSES urban canopy model. Industry is found to be the sector with the highest emissions, with maximum hourly cell values of  $300 \text{ W m}^{-2}$  and  $3500 \text{ W m}^{-2}$  from light and heavy industry, respectively. The second highest emitting sector is non-residential buildings, which can reach maximum hourly grid values of  $350 \text{ W m}^{-2}$  in the central business district. Emissions from residential buildings scale with density and height of buildings, reaching up to  $30 \text{ W m}^{-2}$  in individual cells. The road transport sector reaches maximum hourly cell values of  $60 \text{ W m}^{-2}$  in areas with expressways and the railway network emits up to  $4 \text{ W m}^{-2}$ .

## 1 INTRODUCTION

The anthropogenic heat flux ( $Q_F$ ) is the heat released to the atmosphere by human activities. This heat flux is the sum of the heat released by road traffic ( $Q_V$ ), industries ( $Q_I$ ), residential and non-residential buildings ( $Q_B$ ) and human metabolism ( $Q_M$ ). Hourly  $Q_F$  values can be of similar size or even larger than other terms of the surface energy balance equation (Quah and Roth 2012). This is especially true in commercial or high residential neighbourhoods in certain times of the day. For example, Ichinose et al. (1999) estimated hourly peak values of up to  $908 (1590) \text{ W m}^{-2}$  in central Tokyo during summer (winter). On the other hand, Pigeon et al. (2007) found average seasonal values of up to  $50 (100) \text{ W m}^{-2}$  during summer (winter) in the central area of Toulouse, a medium sized city in the south of France. Oke et al. (2017) shows city wide seasonal values ranging between  $15$  and  $300 \text{ W m}^{-2}$  depending on the size and location of the city and the season, and neighbourhood hourly

values between  $5$  and  $1600 \text{ W m}^{-2}$  depending on the Local Climate Zone (LCZ, Stewart and Oke, 2012).

Numerical studies have shown remarkable impacts on night-time temperature when including  $Q_F$ . Bohnenstengel et al. (2014) found an increase in sensible and latent heat fluxes producing a maximum temperature increase of  $1.5 \text{ K}$  in central parts of London in December when considering  $Q_F$  in their simulations. Another example is found in Fan and Sailor (2005) where  $Q_F$  was found to contribute  $2.5 (0.8) \text{ K}$  to the night-time urban heat island in Philadelphia during winter (summer). These results show the importance of considering  $Q_F$  when simulating the urban environment.

Since  $Q_F$  cannot be directly measured, indirect methods are used to estimate this term. Sailor (2011) distinguished three different approaches: (i) inventory-based approach, (ii) micro meteorologically-based energy budget closure methods and (iii) building energy model-based approaches. While all have their own advantages and limitations, it is important to note that a high level of uncertainty is present in any of them. Inventory-based approaches are based on energy consumption and convert that data into  $Q_F$  release. Two different approaches exist, i.e. bottom-up and top-down, depending on the nature of the data source considered. Two examples of inventory-based  $Q_F$  estimations are Pigeon et al. (2007) and Quah and Roth (2012), although more exist in the literature. The accuracy of the inventory-based approach depends on the space and time resolution of the available data. The energy budget closure method calculates  $Q_F$  as the residual from the measurement of the remaining fluxes of the surface energy balance (SEB) equation, namely net radiation, sensible heat flux, latent heat flux and the heat stored inside buildings and in the soil ( $\Delta Q_S$ ). This method, applied e.g. by Pigeon et al. (2007) and Offerle et al. (2005), has a number of limitations. They include the impossibility to divide the final value between the different sources of  $Q_F$ , the lack of definition of a diurnal profile due to difficulties in properly estimating  $\Delta Q_S$ , or that any potential error during the SEB measuring process would be passed on to  $Q_F$ .

Building energy models aim to estimate the energy consumed by buildings and hence their emission of heat. Although these models are only applied to buildings, they have the advantage of allowing the coupling with an atmospheric model. Examples of such coupling are the studies by Kikegawa et al. (2003), Salamanca et al. (2011) or Bueno et al. (2012). The energy building model from Salamanca et al. (2011) was used in combination with a bottom-up inventory-based approach in Chow et al. (2014) to estimate  $Q_F$  in Phoenix, USA. Finally, models integrating every component of  $Q_F$  also exist in the literature. This is the case for the Large Scale Urban

Consumption of energy model (LUCY, Allen et al. 2010), which computes  $Q_F$  from the global to city scale based on population density, business hours, vehicles fleet and traffic pattern, primary energy and electricity consumption, electricity production and temperature data.

In this work we present an inventory of the  $Q_F$  release in Singapore valid for 2016, based on a combination of top-down and bottom-up approaches. The current study uses a similar methodology to the one presented in Quah and Roth (2012). It extends the geographic region of that

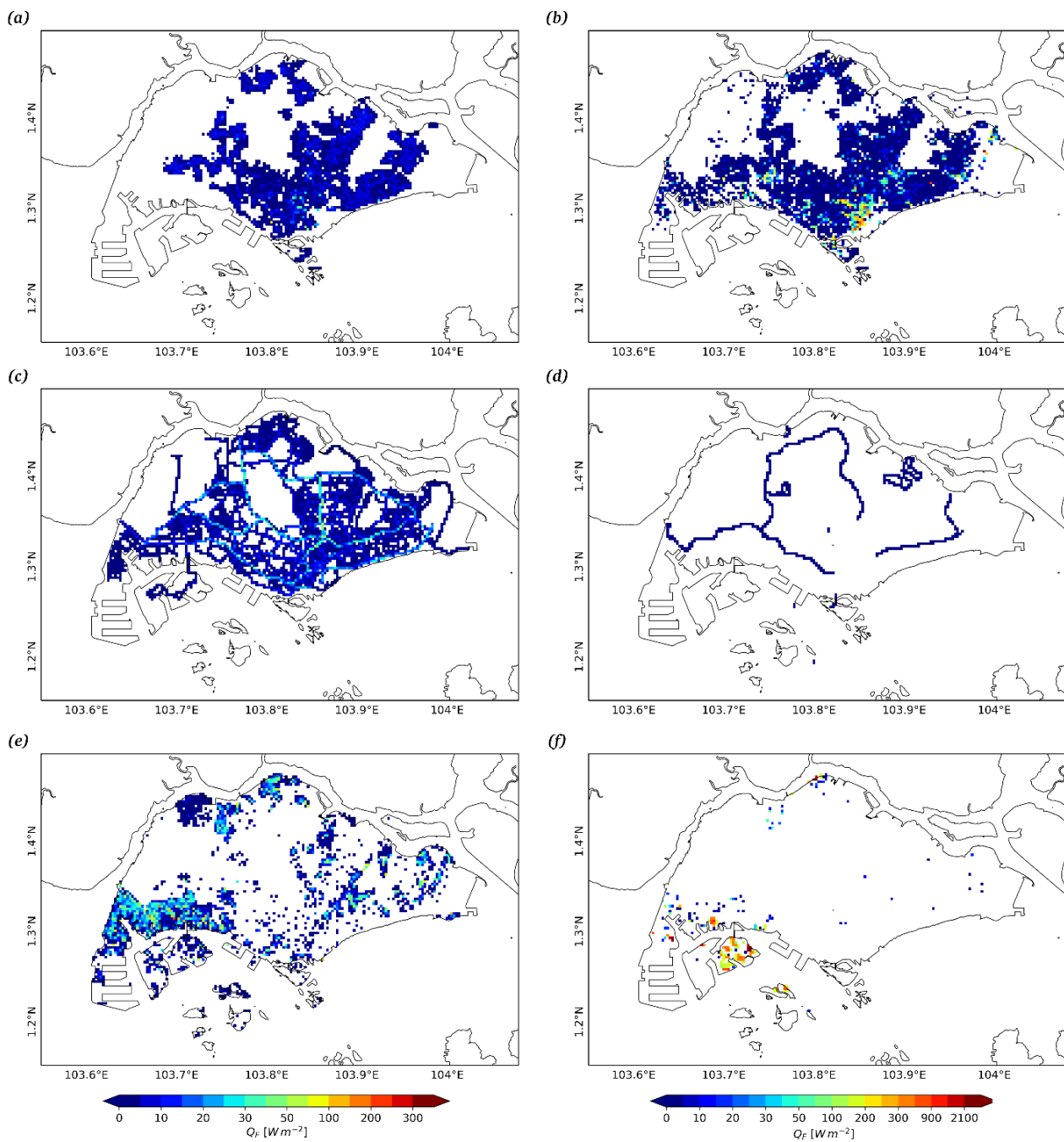


Figure 1: Hourly  $Q_F$  [ $W m^{-2}$ ] by sector. (a) Residential, (b) non-residential, (c) road traffic, (d) railway, (e) light industry and (f) heavy industry. Left colour scale refers to (a)-(e) and right colour scale to (f).

work to include the entire island and also includes the industrial sector, which was not considered previously. The present database is built to be included in the uSINGV model (Simón-Moral et al. 2020, Dipankar et al. 2020, under revision) as part of numerical weather prediction improvement efforts by the Meteorological Service Singapore (MSS).

## 2 METHODOLOGY

An inventory-based estimation of  $Q_F$  release in Singapore is presented here. A combination of bottom-up and top-down approaches is used to calculate the energy consumption based on 2016 information, which is then approximated to  $Q_F$ . While the bottom-up approach uses small scale information (e.g. average household monthly energy consumption) and scales it upward to larger scales, the top-down approach is based on large scale data (e.g. yearly or city scale) and downscales them to smaller scales (Quah, 2012). Emissions from residential and non-residential (commercial) buildings, light and heavy industry, road traffic and railway are considered. Results are presented as hourly averages, calculated by dividing daily totals by 24 hours. A diurnal profile for the calculation of the diurnal evolution of  $Q_F$  is presented at the end. The methodology used for each sector is presented below.

### 2.1 Buildings

We divide the calculation of the building sector into non-residential ( $Q_{B_{NORES}}$ ) and residential ( $Q_{B_{RES}}$ ) buildings. The former category includes every building which is not residential or industrial, such as e.g. hotels, educational buildings, or shopping malls.  $Q_{B_{RES}}$  is further divided in public (Housing and Development Board, HDB) and private housing.

#### 2.1.1 Residential buildings

A bottom-up approach is applied for the calculation of the energy consumed by private and public houses. The energy consumed by a residential building is divided into the energy consumed by the dwellings and the common areas, as:

$$Q_{B_{RES}} = \sum_d n_d E_d + E_{common}$$

Where  $d$  refers to each dwelling type within a building,  $n_d$  and  $E_d$  are the number of and energy consumed (electricity and gas) by dwellings of each dwelling type, respectively, and  $E_{common}$  is the energy consumed by common areas. Monthly electricity consumption (W) by postal code and dwelling type and gas consumption (W)

by dwelling type (averaged across the entire country) for 2016 is provided by the Energy Market Authority (EMA). A georeferenced 3D building database provided by Singapore Land Authority (SLA) is used to assign building properties (e.g. area and height) and location to each postal code. Energy Use Intensity (EUI,  $W m^{-2}$ ) in common areas is taken from Quah (2012).

In order to calculate  $n_d$  in residential buildings, the area of each storey is divided by the average dwelling area of each particular building, considering the percentage of each storey occupied by common areas, and this value is multiplied by the number of storeys. The average dwelling area in public buildings is computed based on the dwelling types per building provided by the EMA database and the area of each dwelling type provided by HDB. The fraction occupied by common areas is estimated based on a selection of floor plans provided by constructors. In the case of private buildings, the area per dwelling is obtained from the Urban Redevelopment Authority Real State Information System (URA-REALIS), by averaging the apartments and condominiums on sale from 2010 to 2014. Corrections were made to the height of buildings in the 3D database as an approximate overestimation of 6 meters was found from individual building inspection carried out with Google Street View.

#### 2.1.2 Non-residential buildings

The energy consumption for non-residential buildings is defined by the EUI of the activity performed inside, identified through a use code provided by the SLA building data base. The building area provided by the SLA buildings database (floor area multiplied by number of storeys) is then multiplied by the corresponding EUI taken from Quah (2012). Assumptions are made in terms of building EUI assignments as not every building use was considered in Quah (2012). These assumptions are made based on similarities in activities performed in each building type. As in the case of residential buildings, the height of each building was corrected.

### 2.2 Industry

The industrial sector is divided in light industry, mostly related to manufacturing activities, and heavy industry, which includes oil refineries, power and incineration plants, industrial combustion and concrete blasting plants. While the manufacturing industry mainly uses electricity, the rest uses diesel, fuel gas, fuel oil or natural gas as fuel sources (National Environment Agency, NEA, 2016). A combination of top-down and bottom-up approaches is used here.

### 2.2.1 Light industry

A top-down approach is applied to calculate the energy consumed by the light industry sector. The yearly electricity consumption by the manufacturing industry provided by the Singapore Energy Statistics 2017 report of the Energy Market Authority (SES, 2017) is divided by the sum of the area of every building dedicated to manufacturing processes. This electricity consumption density is multiplied by each building's area to assign their yearly energy consumption contribution. The yearly value is divided by 365 days and 24 hours to get daily and hourly averages, respectively, not distinguishing between weekdays and weekends. This approximation is done as no further data was available to distinguish between different manufacturing processes or day of the week.

### 2.2.2 Heavy industry

#### 2.2.2.1 Refineries

This subsector converts crude oil into other products, e.g. gasoline, diesel or oil, releasing heat produced in the

process to the air and ocean. Based on SES (2017), refineries used 51.5 Mtoe<sup>1</sup> of crude oil to produce 49.4 Mtoe of distilled products in 2016. The remaining 2.1 Mtoe (24423 GW when converted to energy) is considered as heat release and is divided between the refineries across Singapore, based on their working hours and the sum of the working hours of every refinery, as:

$$Q_{I_{REF}} = \sum_i nh_i \frac{E_T}{365nh_T}$$

where  $nh_i$  is the daily working hours by each refinery plant  $i$ , and  $E_T$  and  $nh_T$  are the total energy released and total working hours by refinery sector, respectively, the latter calculated as the sum of all refinery daily working hours. Location and working hours for each plant are taken from NEA (2016). 20% of the total wasted heat is assumed to be released to the ocean. This conservative estimate is used because of the lack of more detailed information.

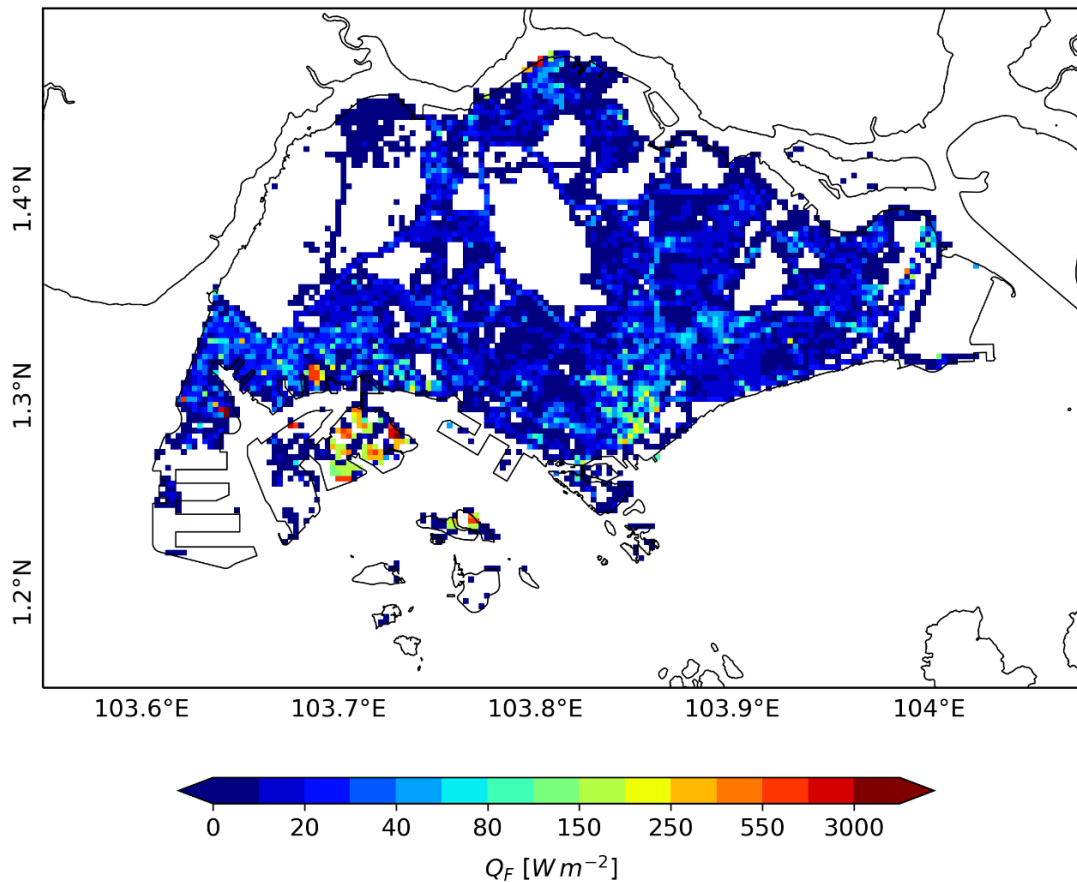


Figure 2: Hourly  $Q_F$  [ $W m^{-2}$ ] from all individual sectors considered in Fig. 1

<sup>1</sup> Megatonne of oil equivalent (Mtoe) is defined as the energy released from burning a megaton of crude oil.

### 2.2.2.2 Power plants

Main power producers (MPP) generated 48299.4 GW in 2016 by converting different fuels (mainly natural gas, coal and petrol) into electricity, releasing heat to the atmosphere. The released heat depends on the efficiency of the technology used. Based on generation capacities, technologies used and market shares by power plant reported in SES (2017), 74% of the power generated by MPP in 2016 was produced by Combined Cycle Gas Turbine plants (CCGTs), Co-Generation Plants and/or Tri-generation Plants (The three referred hereafter as GEN) and 16% by steam turbines (ST). The remaining 10%, which is produced by other technologies, is neglected due to lack of technical information. A mean heat loss of 18.75% is assigned as an approximation for GEN based on information given on the Tuas Power website for Co- and Tri-generation technologies, and 64.05% for ST based on Kumar et al. (2017).

A heat loss of 13768.4 GW from ST plants is estimated with a reverse calculation from the 7727.9 GW (16% of the total) produced by this technology. Based on information given by Tuas Power website, part of the fuel used by GEN plants is transformed into electricity and the remainder is converted to heat, of which part is captured to heat water to produce steam and part is

released to the atmosphere. As the use of the heat captured in the process is not clear, the estimation of the heat loss by GEN is based on the fuel amount used. Considering 89376.6 GW was used by ST and GEN (SES, 2017) and ST used 21496.3 GW, 67880.3 GW was therefore used by GEN, releasing 12727.6 GW to the atmosphere. The results are divided by 365 days to estimate daily values, hence not distinguishing between weekdays and weekends.

These values are distributed across plants based on their locations (NEA, 2016), technology used, and percentage of total electricity produced by each plant (Table 1). Note that only MPPs are considered as the location and capacities of auto producers are not available. Of the MPPs, Pacific Light and Tuaspring chimney locations are not provided. Hence, they are not considered; which, however, is an omission of only about 12.4% of the total power generated in Singapore (Table 1).

### 2.2.2.3 Incineration, industrial combustion and concrete batching/grift blasting plants

The heat released by the rest of the heavy industry sub sector is computed based on the methodology presented in Lee et al. (2014) and adapted for Korea by Koralegedara et al. (2016). Accordingly heat release is estimated as a function of CO and NO<sub>x</sub> emissions, as:

Name	% of total	% GEN	% ST
Tuas Power Generation Pte Ltd	21	76.7	23.3
Senoko Energy Pte Ltd	19.2	85.0	15
YTL PowerSeraya Pte Ltd	17.7	47.5	46.7
Keppel Merlimau Cogen. Pte Ltd	10.4	100.0	-
SembCorp Cogen Pte Ltd	10.4	100.0	-
PacificLight Power Pte Ltd	8.8	100.0	-
Tuaspring Pte Ltd	3.6	100.0	-
Others	9	-	-

**Table 1: Name of power generation plant, percentage of total energy produced and partitioning according to technology used. GEN accounts for CCGT, Co- and Tri- generation plants and ST for Steam turbines plants. Source: Singapore Energy Statistics, 2017.**

$$Q_{Inc} = 0.5(2.55X_{CO}^{0.64}) + 0.5(3.71X_{NOx}^{0.69})$$

where  $X_{CO}$  and  $X_{NOx}$  are the hourly averaged emissions of CO and NOx in  $\text{kg km}^{-2} \text{h}^{-1}$ , respectively. Data of emissions and locations are obtained from NEA (2016).

### 2.3 Traffic

The heat released by road motor vehicles is calculated based on Grimmond (1992) as:

$$Q_V = \sum_{ijk} (n_{vij} EV_{ij} d_k) / 3600$$

$$EV_{ij} = (NHC_j \rho_j) / FE_{ij}$$

where the subscripts  $i, j$  and  $k$  refer to vehicle class, fuel type and road segment, respectively,  $n_{vij}$  is the daily number of vehicles of class  $i$ , consuming fuel type  $j$  on road segment  $k$ ,  $d_k$  is the distance travelled on  $k$ ,  $EV_{ij}$  is the energy used per vehicle of class  $i$  and fuel type  $j$ ,  $NHC_j$  is the net heat combustion of fuel  $j$ ,  $\rho_j$  is the density of the fuel type  $j$  and  $FE_{ij}$  is the mean fuel economy of vehicles of class  $i$  and fuel type  $j$ .

Traffic count information by road segment from 2013 (bottom-up approach) and a generalized island wide vehicle types breakdown per road segment (top-down) is used to calculate the number of each vehicle type on each road segment (NEA, 2016). Data from 2013 is used here because of data availability.  $NHC_j$ ,  $\rho_j$  and  $FE_{ij}$  are taken from Quah and Roth (2012). The distribution of vehicle types per road segment doesn't distinguish between fuel types or engine displacement, therefore the 2016 national fleet data generated by the Land Transport Authority published by Singapore government data portal is used for further disaggregation. While each vehicle type mostly uses one single fuel type (e.g. 96% of cars use petrol and 95% of commercial vehicles use diesel), cars are further divided according to their engine size as  $>1600 \text{ cc}$  (45%) and  $< 1600 \text{ cc}$  (55%).

### 2.4 Railway

The transport related electricity consumption published in SES (2017) is used to estimate the heat released by the railway system (Mass Rapid Transit, MRT) via a top-down approach. The yearly value for 2016 which was 2639.4 GWh and the georeferenced rail network are used to define an electricity consumption density which is assigned to every network segment. The energy consumed by subway trains is divided into the energy consumed by engines, auxiliary systems (e.g. air conditioning, lights, etc) and brakes (Villalba Sanchís et

al. 2016). The breakdown of the total consumption is 72.5, 22.5 and 5%, respectively (Ignacio Villalba Sanchís, personal communication). From this breakdown, we consider that the engines are 98% efficient and we approximate the heat released from brakes and auxiliary systems to the energy consumed, hence 28.95% of the total consumed energy is released as heat. In addition, part of the network is below ground level, so the heat is not entirely released to the atmosphere, being mostly contained within the tunnels. Due to a lack of information about how much of the underground released energy escapes to the atmosphere, only the segments above ground are accounted for.

### 2.5 Diurnal cycle

A diurnal profile based on hourly data is defined and applied equally across the island. This diurnal profile is calculated as an average of the three diurnal profiles presented in Quah and Roth (2012) for residential, mixed commercial-residential and commercial areas, respectively. The averaged diurnal profile does not represent industry and more work is therefore needed to define a diurnal profile for each sector.

## 3 RESULTS

The methodology described above is applied to a 300 x 300 m resolution grid covering most of Singapore. Results grouped by sectors are presented in Fig. 1. The sum of all sectors is shown in Fig. 2 and the diurnal profile is depicted in Fig. 3.

The residential sector contributes to total hourly  $Q_F$  with 11809.3  $\text{W m}^{-2}$ . The highest grid-cell values range between 20 and 30  $\text{W m}^{-2}$  and are found in the centre south of the island, where there is a higher concentration of high-rise private apartments (Fig. 1a). Relatively high values are also found in the northeast of the island, mainly due to the contribution of HDB developments. Areas with zero or very low values correspond to nature reserves, big parks, airports and industries (Fig. 1e and f).

Non-residential buildings contribute 22811.5  $\text{W m}^{-2}$  to the hourly total and are spread across most of Singapore. The highest grid-cell  $Q_F$  (150 – 350  $\text{W m}^{-2}$ ) can be found in the commercial and business districts located in the south of the island (Fig. 1b). Other secondary maxima are located in areas with a high concentration of shopping malls. The main contribution in those areas comes from the extensive use of air conditioning (Quah and Roth, 2012).

Traffic contributes  $21764.0 \text{ W m}^{-2}$  to the hourly total  $Q_F$ . Grid-averaged values along highways and major roads range between  $20$  and  $60 \text{ W m}^{-2}$  (Fig. 1c). Smaller roads, closer to residential and commercial areas release approximately  $5$  to  $15 \text{ W m}^{-2}$ . The MRT network contributes  $418.5 \text{ W m}^{-2}$  to the hourly total. Maximum grid-cell values are  $\sim 4 \text{ W m}^{-2}$ , with the majority of cells contributing  $\sim 1 \text{ W m}^{-2}$  (Fig. 1d).

The industrial sector, primarily located in the southwest and some areas of the north and northeast, is responsible for the largest  $Q_F$  contribution. The light industrial subsector releases an hourly total of  $26611.5 \text{ W m}^{-2}$ , with some grid-cell values reaching  $200\text{--}300 \text{ W m}^{-2}$  (Fig. 1e). Heavy industry releases an hourly total of  $59138.0 \text{ W m}^{-2}$  and can reach individual cell values of up to  $3500 \text{ W m}^{-2}$  (Fig. 1f). It is important to note that heavy industry releases from chimneys are averaged across high resolution  $300 \times 300 \text{ m}$  grid-boxes, hence resulting in higher  $Q_F$  values than what was obtained in a study for Brisbane, Australia, using a lower resolution approach (Khan and Simpson (2001), with similar or even lower total  $Q_F$ .

## 4 DISCUSSION

A high-resolution inventory based  $Q_F$  database for Singapore is presented in this research letter. The contributions of residential and non-residential

buildings, road traffic, railway, light and heavy industrial sectors are considered separately and in total. Based on data availability, different methodologies are used to estimate contributions from each sector.

The industrial sector has been found to contribute the most to the total  $Q_F$  release, especially in the case of the heavy industry. The values obtained for the latter are larger than the ones obtained in other studies, e.g. Khan and Simpson (2001). Part of this difference can be explained by the higher resolution used here compared to the  $2 \text{ km}$  used in their study. The second highest contribution is from the non-residential building sector which includes shopping malls, offices and other services. Traffic has been found to contribute more than the residential sector in total values. Overall, the results obtained in every sector agree with the ones presented in Oke et al. (2017).

One of the main limitations of the present inventory is the lack of inclusion of human metabolism. It has not been considered due to the inherent difficulty to provide an accurate island-wide estimation. However, this component accounts only for  $\sim 5\text{--}20\%$  of the total  $Q_F$  release, depending on the neighbourhood (residential or commercial) and whether it is a weekday or weekend (Quah and Roth, 2012).

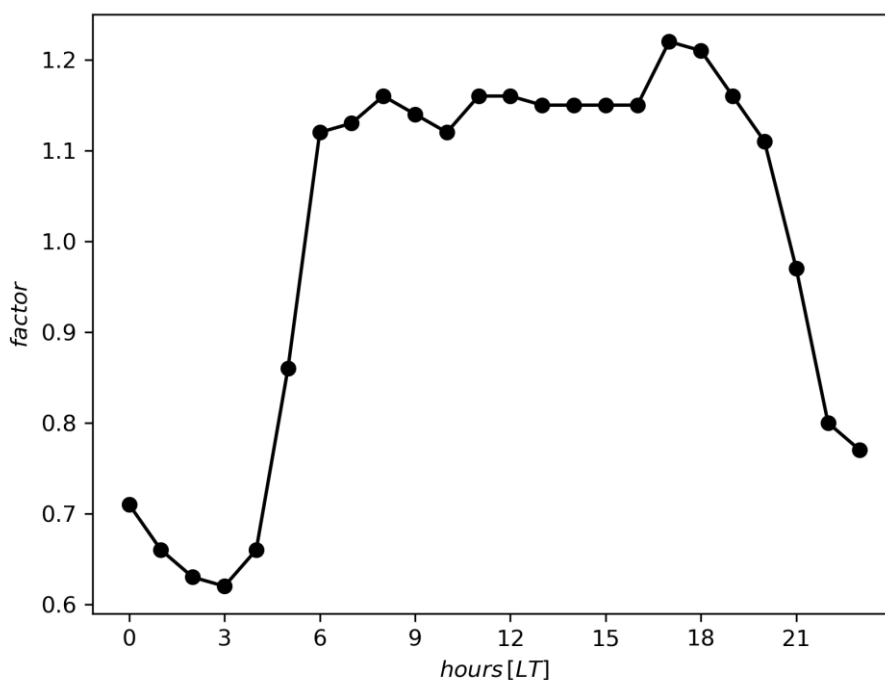


Figure 3: Diurnal profile of the dimensionless factor to obtain hourly  $Q_F$ .

Two other limitations are the consideration of a single diurnal profile for the entire island and the lack of differentiation between weekdays and weekends. The reason for not defining an activity- or day-related diurnal profile is a model limitation, as the final goal of the present work is to provide an input for the uSINGV model. Therefore, this inventory needs further improvements in order to be used for other purposes or to be implemented in more sophisticated urban models.

## 5 REFERENCES

- Allen, L., Lindberg, F. and Grimmond, C. (2011) 'Global to city scale urban anthropogenic heat flux: model and variability', *International Journal of Climatology*, 31: 1990-2005. doi:[10.1002/joc.2210](https://doi.org/10.1002/joc.2210)
- Bohnenstengel, S., Hamilton, I., Davies, M. and Belcher, S. (2014) 'Impact of anthropogenic heat emissions on London's temperatures', *Quarterly Journal of the Royal Meteorological Society*, 140, 687–698. <https://doi.org/10.1002/qj.2144>.
- Bueno, B., Pigeon, G., Norford, L., Zibouche, K. and Marchadier, C. (2012) 'Development and evaluation of a building energy model integrated in the TEB scheme', *Geosci. Model Dev.*, 5, 433–448, <https://doi.org/10.5194/gmd-5-433-2012>, 2012.
- Chow, W., Salamanca F., Georgescu, M., Mahalov, A., Milne, J., Ruddell, B. (2014) 'A multi-method and multi-scale approach for estimating city-wide anthropogenic heat fluxes', *Atmospheric Environment*, 99, 64-76, <https://doi.org/10.1016/j.atmosenv.2014.09.053>.
- Dipankar, A., Webster, S., Furtado, K., Wilkinson, J., Sánchez, C., Lock, A., North, R., Sun, X., Vosper, S., Huang, X.-Y. and Barker, D. (2020) 'SINGV: a convective-scale weather-forecast model for Singapore', *Quarterly Journal of the Royal Meteorological Society*. (under revision)
- Fan, H. and Sailor, D. (2005) 'Modeling the impacts of anthropogenic heating on the urban climate of Philadelphia: a comparison of implementations in two PBL schemes', *Atmospheric Environment* 39: 73–84.
- Grimmond, C. (1992) 'The suburban energy-balance – methodological considerations and results for a mid-latitude west coast city under winter and spring conditions', *International Journal of Climatology* 12: 481–497.
- Ichinose, T., Shimodozono, K., Hanaki, K. (1999) 'Impact of anthropogenic heat on urban climate in Tokyo', *Atmospheric Environment* 33(24): 3897–3909.
- Khan, S. and Simpson, R. (2001) 'Effect Of A Heat Island On The Meteorology Of A Complex Urban Airshed', *Boundary-Layer Meteorology* 100, 487–506 (2001). <https://doi.org/10.1023/A:1019284332306>
- Kikegawa, Y., Genchi, Y., Yoshikado, H., Kondo, H. (2003) 'Development of a numerical simulation system toward comprehensive assessments of urban warming countermeasures including their impacts upon the urban buildings' energy-demands', *Applied Energy* 76: 449–466.
- Koralegedara, S., Lin, C-Y., Sheng, Y-F., Kuo, C-H. (2016), 'Estimation of anthropogenic heat emissions in urban Taiwan and their spatial patterns', *Environ. Pol.*, 215, 84-95, <https://doi.org/10.1016/j.envpol.2016.04.055>.
- Kumar, V., Pandya, B., Matawala, V. (2018) 'Thermal comparison and multi-objective optimization of single-stage aqua-ammonia absorption cooling system powered by different solar collectors', *Journal of Thermal Analysis and Calorimetry* 133:3, 1635-1648.
- Lee, S., McKeen, S., Sailor, S. (2014) 'A regression approach for estimation of anthropogenic heat flux based on a bottom-up air pollutant emission database', *Atmospheric Environment*, 95, 629-633, <https://doi.org/10.1016/j.atmosenv.2014.07.009>.
- National Environment Agency (2016) 'Consultancy Study on Emissions Inventory for Air Pollutants in Singapore for Year 2013'. Technical report.
- Offerle, B., Grimmond, C., Fortuniak, K. (2005) 'Heat storage and anthropogenic heat flux in relation to the energy balance of a central European city centre', *International Journal of Climatology* 25: 1405–1419
- Oke, T., Mills, G., Christen, A. and Voogt, J. (2017) 'Urban Climates', Cambridge: Cambridge University Press.
- Pigeon, G., Legain, D., Durand, P. and Masson, V. (2007) 'Anthropogenic heat release in an old European agglomeration (Toulouse, France)', *International Journal of Climatology* 27: 1969–1981.
- Quah, A. (2012) 'Diurnal and weekly variation of anthropogenic heat emissions in Singapore', Master's Thesis, National University of Singapore, 172 p.

Quah, A. and Roth, M. (2012) 'Diurnal and weekly variation of anthropogenic heat emissions in a tropical city, Singapore', *Atmospheric Environment*, 46, 92–103. <https://doi.org/10.1016/j.atmosenv.2011.10.015>.

Sailor, D.J. (2011) 'A review of methods for estimating anthropogenic heat and moisture emissions in the urban environment', *Int. J. Climatol.*, 31: 189-199. doi:[10.1002/joc.2106](https://doi.org/10.1002/joc.2106)

Salamanca, F., Martilli, A., Tewari, M., and Chen, F. (2011) 'A Study of the Urban Boundary Layer Using Different Urban Parameterizations and High-Resolution Urban Canopy Parameters with WRF', *Journal of Applied Meteorology and Climatology*, 50(5), 1107–1128. <https://doi.org/10.1175/2010jamc2538.1>

Simón-Moral, A., Dipankar, A., Roth, M., Sanchez, C., Velasco, E. and Huang, X-Y. (2020) 'Application of MORUSES single-layer urban canopy model in a tropical city: Results from Singapore', *Quarterly Journal of the Royal Meteorological Society*, 146: 576 – 597. <https://doi.org/10.1002/qj.3694>

Singapore Energy Statistics (2017). Singapore: Energy Market Authority. <http://www.ema.gov.sg>

Stewart, I. and Oke, T. (2012) 'Local Climate Zones for urban temperature studies', *Bulletin of the American Meteorological Society*, 93: 1879 - 1900. <https://doi.org/10.1175/BAMS-D-11-00019.1>

Villalba Sanchis, I. and Salvador Zuriaga, P. (2016) 'An Energy-efficient Metro Speed Profiles for Energy Savings: Application to the Valencia Metro', *Transportation Research Procedia*, 18, 226-233, <https://doi.org/10.1016/j.trpro.2016.12.031>.

---

## GLOSSARY

**Anthropogenic heat flux (QF):** A measure of heat released to the atmosphere by human activities. This heat flux is the sum of the heat released by road traffic (QV), industries (QI), residential and non-residential buildings (QB) and human metabolism (QM).

**Clearness index:** A measure of the atmospheric transmissivity of solar irradiance. It is defined as the observed GHI at a station divided by the incoming solar irradiance assuming the atmosphere is absent.

**Cloud Cover:** Cloud observations recorded hourly by human observers based on guidelines specified in the International Cloud Atlas published by the World Meteorological Organization (WMO). The amount of cloud cover is reported in the unit of oktas with values ranging from 0 to 8 (WMO, 1975, 1987).

**Confidence Levels:** Measures given by the NOAA-20 active fire product that are used to assess the likelihood of false detections of hotspots. The Confidence Levels of the algorithm are a heuristic measure determined by the number of adjacent cloud pixels, adjacent water pixels, and temperature thresholds.

**Energy Use Intensity (EUI):** The energy consumption for non-residential buildings is defined by the EUI of the activity performed inside, identified through a use code provided by the SLA building data base.

**European Centre for Medium-range Weather Forecasts (ECMWF):** A research institute and operational NWP centre dedicated to improving forecasts in the 7 to 15-day window. Besides medium-range forecasts, it also provides additional forecasts such as those at the sub-seasonal to seasonal timescale.

**Fire Radiative Power (FRP):** A measure of the rate of radiant heat output from a fire.

**Global Horizontal Irradiance (GHI):** A measure of the irradiance received by solar panels.

**Numerical Weather Prediction (NWP):** Computer models that solve mathematical equations representing atmospheric physics. Used extensively in weather forecasting.

**PM10 concentration:** Defined as the total mass per unit air of aerosol particles with diameters of 10  $\mu\text{m}$  or smaller.

**Regional Climate Models (RCMs):** Similar to global climate models, but run for a region (or limited area) in order to achieve a finer resolution.

**Singapore Land Authority (SLA):** A statutory board under the Ministry of Law of the Singapore Government focusing on land resource optimization. It has 2 main roles: developmental and regulatory.

**Singapore Variable Resolution- Data Assimilation (SINGV- DA):** MSS's integrated regional data assimilation based numerical weather prediction system, developed jointly in collaboration with the UK Met Office.

**Surface solar irradiance:** Also known as global radiation, it is the solar radiation flux on a horizontal earth surface; it is expressed in  $\text{Wm}^{-2}$ .

**Urban Heat Islands (UHIs):** An urban or built up area that is considerably warmer than the surrounding areas.

Visible Infrared Imaging Radiometer Suite (VIIRS): A sensor designed and manufactured by the Raytheon Company on board the Suomi National Polar-orbiting Partnership (Suomi NPP) and NOAA-20 weather satellites. VIIRS is one of five key instruments on board Suomi NPP, launched on October 28, 2011.

World Meteorological Organisation (WMO): An agency under the United Nations for meteorology (both weather and climate), as well as operational hydrological services.



*Website: [ccrs.weather.gov.sg](http://ccrs.weather.gov.sg)*

*Address: 36 Kim Chuan Road, Singapore 537054*